Activation of Conductive Pathways via Deformation-induced Instabilities

by

Xinchen Ni

B.S. Mechanical Engineering

Fudan University, Shanghai, China 2012

Submitted to the Department of Mechanical Engineering

in partial fulfillment of the requirements for the degrees of

Master of Science in Mechanical Engineering

at the

Massachusetts Institute of Technology

June 2014

Signature redacted

Author.....

Department of Mechanical Engineering
May 13, 2014

Signature redacted

Certified by.....

Mary C. Boyce
Ford Professor of Mechanical Engineering
Thesis Supervisor

Signature redacted

Accepted by.....

David E. Hardt
Ralph E. and Eloise F. Cross Professor of Mechanical Engineering
Chair, Department Committee on Graduate Students

Activation of Conductive Pathways via Deformation-induced Instabilities

by

Xinchen Ni

Submitted to the Department of Mechanical Engineering
on May 13, 2014, in partial fulfillment of the
requirements for the degree of
Master of Science in Mechanical Engineering

Abstract

Inspired by the pattern transformation of periodic elastomeric cellular structures, the purpose of this work is to exploit this unique ability to activate conductive via deformation-induced instabilities. Two microstructural features, the contact nub and the conductive pathway, are introduced to make connections within the void and between the voids upon pattern transformation. Finite element-based micromechanical models are employed to investigate the effects of the contact nub geometries, conductive pathway patterns and elastic properties of the coating and substrate materials on the buckling responses of the structure. Finally, a flexible circuit that can be switched on and off by an applied uniaxial load is fabricated based on the finite element analysis and demonstrated the ability to activate conductive pathways in response to an external triggering stimulus.

Thesis Supervisor: Mary C. Boyce
Title: Ford Professor of Mechanical Engineering

Acknowledgements

First and foremost, I would like to express my deepest appreciation to my adviser, Professor Mary C. Boyce. To think upon where I started from two years ago, and how far I have come since then, I feel extremely grateful to have you as my mentor. Your patience, kindness and knowledge have helped me to develop into the person I am now. I wish you all the best at your new future at Columbia University and I will always be proud of being your student.

I would also like to thank everyone in the Boyce's lab. Thank you, Stephan for your guidance along the way. Thank you, Hansohl for all the coffee break and late night chats. Thank you, Narges for treating me as your little brother. Thank you, Mark for always being funny and positive. Thank you, Erica for all the tutoring on Zwick. Thank you, Shabnam and Swati for always being patient and answering my questions. I also like to thank Juliette, Leslie, Joan and Una for making administrative matter much easier.

Above all, I would like to thank my friends and family for all your love and support. Thank you, Ke, for being with me and supporting me through all the ups and downs. I am so grateful to have you and I promise that I will do the same thing to you. Thank you, Mom and Dad. There are really no words to describe how grateful I am and how much I love you. I know you have scarified so much to help me to get to where I am right now. Yes, your son has got a degree from MIT and he will keep working hard to realize his dream. But I want to tell you that no matter where I am and no matter what I do, my love is always with you.

Table of Contents

List of Figures

Chapter 1
Introduction

Periodic microstructures abound in nature and demonstrate numerous interesting and unique mechanical, photonic and hydrophobic properties.

In recent years, a number of research groups have focused on periodic elastomeric structures because of their unique ability to switch between two very different configurations due to instability in response to an external triggering stimulus. These structures offer exciting opportunities to design lightweight responsive and reconfigurable devices that have a wide range of applications in sensors, bioengineering, microfluidics and photonics. For example, photonic switches could be created to filter waves if the periodic pattern length scales are in the order of the wavelength of light.

In this chapter, an overview of state-of-the-art research on periodic elastomeric structures is presented, and the objective of this study is proposed at the end.

1.1 Overview of periodic elastomeric structures and their applications

1.1.1 Phononic and photonic crystals

Phononic and photonic crystals are periodic structures that are capable of controlling the propagation of waves through band gaps: a range in frequency where wave propagation is barred [1]. Phononic crystals have exciting applications such as sound filters, acoustic wave guides, and vibration isolators; Photonic crystals avenues to control light waves such as tuning colors and directing light. Figure 1.1(a) shows an image of an opal bracelet. It is essentially a natural photonic crystal with periodic microstructures that give rise to its iridescent color. Figure 1.1(b) illustrates the concept of a phononic band gap. The yellow region in the picture represents a frequency range where sound wave propagation is forbidden [1].

It is desirable to design tunable photonic and phononic band gap systems because most photonic and phononic crystals only operate at a fixed frequency range. Great advances have

been made towards this goal using methods such as altering out-of-plane modes with piezoelectric effects [2] and directly physically changing the positioning of the periodic structure [3]. The dramatic shape change of periodic patterned elastomeric structures due to instability also provides one potential alternative: to use deformation and other stimulus as an external means to control band gaps in photonic and phononic crystals [4]. Figure 1.1(c) demonstrates this idea. It shows the different band gaps of a 2D periodic elastomeric structure with a square array of circular voids at different strain levels.

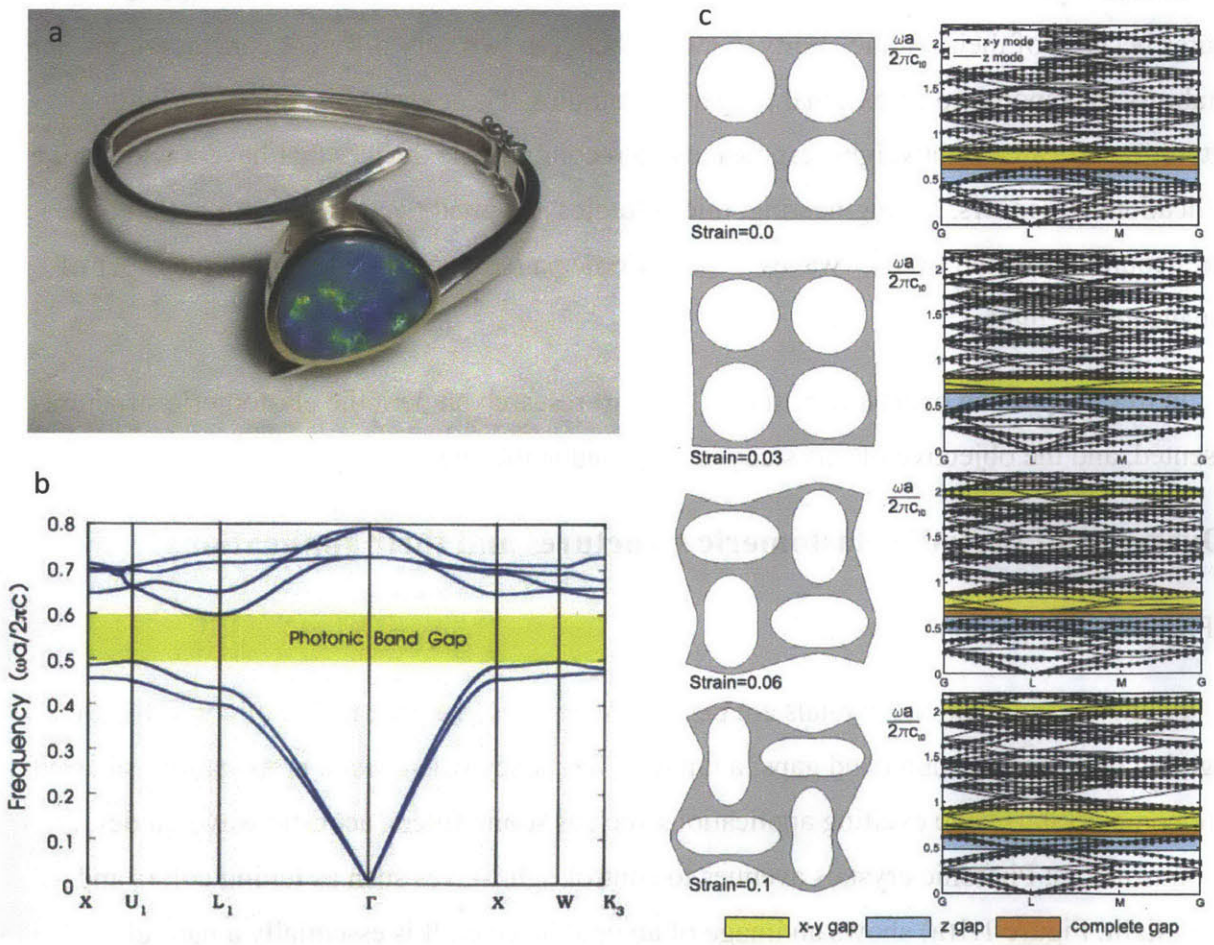

Figure1.1 (a) Image of an opal bracelet, a natural photonic crystal (Taken from Wikipedia) (b) Demonstration of a photonic band gap [1] (c) Phononic band gaps for a 2D periodic structures with a square array of circular holes at different strains (Taken from Bertoldi and Boyce 2008 [4])

1.1.2 Auxetic materials

Mechanical instability of periodic patterned elastomeric structures can also be used to design 3D metamaterials with switchable Poisson's ratio. The Poisson's ratio is defined as the ratio between the transverse and axial strain when subjected to uniaxial stresses [5]. When compressed, most materials expand outwards in the directions orthogonal to the applied load resulting in a positive Poisson's ratio. However, the pattern transforming material of Mullins, Boyce et al. [6] was demonstrated to have a Possion's ratio that transforms from a positive Possion's ratio to a negative Possion's ratio after the deformation-induced pattern transformation [7], [8].

Figure 1.2 shows a periodic patterned structure with a square array of circular holes. When the structure is uniaxially compressed, a structural transformation induced by instabilities occurs [8], [9] and the initial circular holes transform into elongated, almost closed ellipses, giving rise to the shrinkage of the entire structure. Moreover, a significant lateral contraction is observed and is further accentuated with the increase of applied strain. This material behavior offers great potential for designing energy absorbing devices.

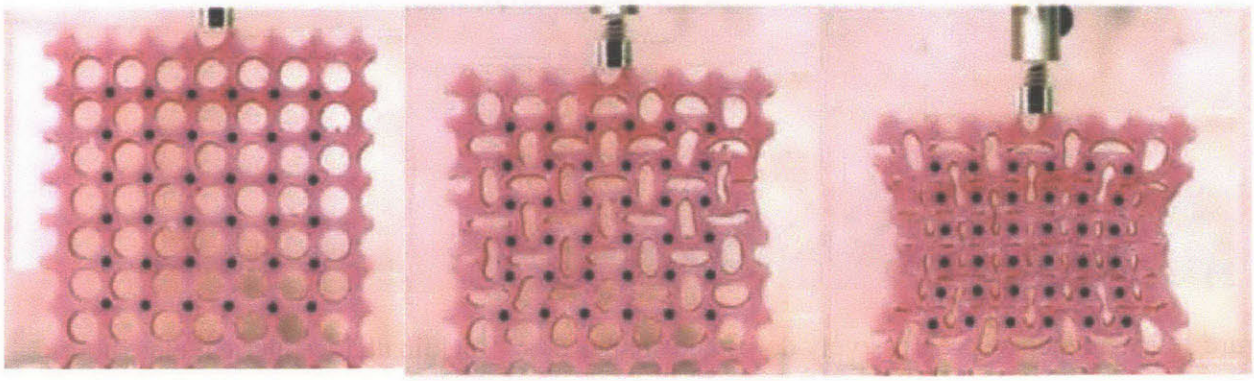

Figure 1.2 Images of the progressive deformation of an elastomeric matrix comprising a square array of circular holes (Taken from Overvelde, Shan et al. 2012 [10])

1.1.3 Soft origami-like structure

The attractive characteristics of periodic elastomeric structures also provide routes for the fabrication of foldable and origami-like structures that have a wide range of applications such as drug delivery capsules [11], material synthesis agents and soft-material robots [12].

One interesting example of a 3D origami-like structure is shown in Figure 1.3. It was developed by Professor Pedro Reis's group at MIT and Professor Katia Bertoldi's group at Harvard and is based on the pattern transforming structure of Mullins et al. [6] The structure is named the "Buckliball" because the shape change is a result of local buckling of ligaments in the structure. The "Buckliball" comprises a spherical elastomeric shell patterned with 24 carefully spaced dimples. The inner pressure is controlled by a motorized syringe pump. When air is sucked out of the ball, the thin ligaments between the dimples buckle, inducing a "cooperative buckling cascade" of the skeleton of the ball in the same manner as the planar cases of Mullins et al. [6], [13]. As a result, the circular dimples turn into ellipses that are almost closed and the ball volume is reduced by up to 54%. Moreover, the structure remains spherical throughout the process. Figure 1.3 shows the progressive images of the deformation.

A big advantage of the buckling-induced folding mechanism of the elastomeric structures is that it is fully reversible and can be achieved without moving parts. This opens the possibility for reversible encapsulation over a wide range of length scales.

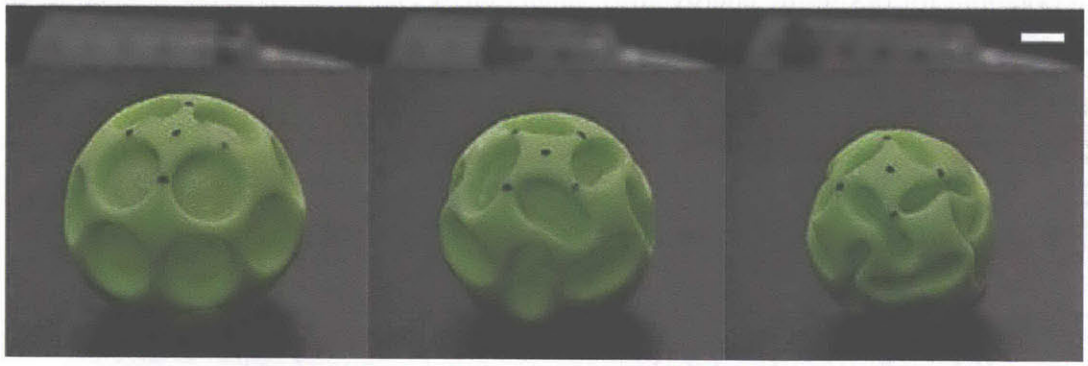

Figure 1.3 Sequence of progressively deformed shapes of a "Buckliball," a spherical elastomeric shell patterned with a regular array of circular voids, due to the decrease of internal pressure (Taken from Shim, Perdigou et al. 2012 [13])

1.2 Thesis objective

Great advances have been made to take advantage of the reversible and dramatic pattern transformation of periodic elastomeric structures, such as the tunable phononic crystals and the Buckliball for encapsulation. Moreover, while there have been extensive works on the effect of topology on the behaviors of periodic elastomeric structures [7], [10], [14], [15] as well as the

stretchability of thin films on elastomeric substrates [16], [17], little has been investigated on the overall buckling and postbuckling behavior of the elastomer when it is periodically patterned with another material.

In this thesis, a flexible circuit with switchable conductive pathways that can be controlled by deformation-induced instabilities is designed based on finite element analysis. Also, 3D printed electronics techniques are exploited to fabricate a working demonstration circuit.

A major challenge of the design is to make connections between the voids of the continuous porous structure as it undertakes a dramatic shape change induced by instabilities. Here, we first introduce two novel design concepts of contact nubs and conduction pathways. We then choose an optimal geometry of those features based on finite element analysis and confirm our design with experiments. Finally, we present a robust flexible circuit harnessing the optimized elastomeric substrate geometries that is fabricated using 3D printing techniques and stretchable conductive ink.

1.3 References

[1] J. D. Joannopoulos, S. G. Johnson, J. N. Winn, and R. D. Meade, Photonic Crystals: Molding the Flow of Light (Second Edition) (Google eBook). Princeton University Press, 2011, p. 304.

[2] Z. Hou, F. Wu, and Y. Liu, "Phononic crystals containing piezoelectric material," Solid State Commun., vol. 130, no. 11, pp. 745–749, Jun. 2004.

[3] Y. Yao, Z. Hou, and Y. Liu, "The two-dimensional phononic band gaps tuned by the position of the additional rod," Phys. Lett. A, vol. 362, no. 5–6, pp. 494–499, Mar. 2007.

[4] K. Bertoldi and M. C. Boyce, "Wave propagation and instabilities in monolithic and periodically structured elastomeric materials undergoing large deformations," Phys. Rev. B, vol. 78, no. 18, 2008.

[5] G. N. Greaves, A. L. Greer, R. S. Lakes, and T. Rouxel, "Poisson's ratio and modern materials.," Nat. Mater., vol. 10, no. 11, pp. 823–37, Nov. 2011.

[6] T. Mullin, S. Deschanel, K. Bertoldi, and M. Boyce, "Pattern Transformation Triggered by Deformation," Phys. Rev. Lett., vol. 99, no. 8, p. 084301, Aug. 2007.

[7] S. Babaee, J. Shim, J. C. Weaver, E. R. Chen, N. Patel, and K. Bertoldi, "3D Soft Metamaterials with Negative Poisson's Ratio," Adv. Mater., vol. 25, no. 36, pp. 5044–5049, 2013.

[8] K. Bertoldi, P. M. Reis, S. Willshaw, and T. Mullin, "Negative Poisson's Ratio Behavior Induced by an Elastic Instability," Adv. Mater., vol. 22, no. 3, p. 361–+, 2010.

[9] K. Bertoldi, M. C. Boyce, S. Deschanel, S. M. Prange, and T. Mullin, "Mechanics of deformation-triggered pattern transformations and superelastic behavior in periodic elastomeric structures," J. Mech. Phys. Solids, vol. 56, no. 8, pp. 2642–2668, 2008.

[10] J. T. B. Overvelde, S. Shan, and K. Bertoldi, "Compaction through buckling in 2D periodic, soft and porous structures: effect of pore shape.," Adv. Mater., vol. 24, no. 17, pp. 2337–42, May 2012.

[11] Y. Zhu, J. Shi, W. Shen, X. Dong, J. Feng, M. Ruan, and Y. Li, "Stimuli-responsive controlled drug release from a hollow mesoporous silica sphere/polyelectrolyte multilayer core-shell structure.," Angew. Chem. Int. Ed. Engl., vol. 44, no. 32, pp. 5083–7, Aug. 2005.

[12] C. Laschi, M. Cianchetti, B. Mazzolai, L. Margheri, M. Follador, and P. Dario, "Soft Robot Arm Inspired by the Octopus," Adv. Robot., vol. 26, no. 7, pp. 709–727, Jan. 2012.

[13] J. Shim, C. Perdigou, E. R. Chen, K. Bertoldi, and P. M. Reis, "Buckling-induced encapsulation of structured elastic shells under pressure.," Proc. Natl. Acad. Sci. U. S. A., vol. 109, no. 16, pp. 5978–83, Apr. 2012.

[14] S. H. Kang, S. Shan, W. L. Noorduin, M. Khan, J. Aizenberg, and K. Bertoldi, "Buckling-induced reversible symmetry breaking and amplification of chirality using supported cellular structures.," Adv. Mater., vol. 25, no. 24, pp. 3380–5, Jun. 2013.

[15] S. Singamaneni, K. Bertoldi, S. Chang, J.-H. Jang, S. L. Young, E. L. Thomas, M. C. Boyce, and V. V. Tsukruk, "Bifurcated Mechanical Behavior of Deformed Periodic Porous Solids," Adv. Funct. Mater., vol. 19, no. 9, pp. 1426–1436, May 2009.

[16] T. Li and Z. Suo, "Deformability of thin metal films on elastomer substrates," Int. J. Solids Struct., vol. 43, no. 7–8, pp. 2351–2363, 2006.

[17] T. Li, Z. Huang, Z. Suo, S. P. Lacour, and S. Wagner, "Stretchability of thin metal films on elastomer substrates," Appl. Phys. Lett., vol. 85, no. 16, p. 3435, Oct. 2004.

Chapter 2
Background

In this chapter, we first characterize the material behavior of the silicone rubber we use throughout the study. Then, the method of periodic boundary conditions as a means for modeling periodic structures and Refined Eigen Analysis are introduced. The former is useful for analyzing large structures with repeating units, while the latter is a typical approach to explore the instability of structures.

2.1 List of symbols

We use standard notation of modern continuum mechanics throughout this work, which is listed below.

$\mathbf{X}$	Material point in the reference body
$\mathbf{x}$	Spatial point in the deformed body
$\mathbf{x} = \boldsymbol{\chi}(\mathbf{X}, t)$	Motion function
$\mathbf{F} = \nabla\boldsymbol{\chi}$	Deformation gradient
$J = \det\mathbf{F} > 0$	Determinant of $\mathbf{F}$
$\mathbf{u} = \mathbf{x} - \mathbf{X}$	Displacement
$\mathbf{H} = \nabla\mathbf{u}$	Displacement gradient
$\mathbf{F} = \mathbf{RU} = \mathbf{VR}$	Polar decomposition of $\mathbf{F}$
$\mathbf{U}, \mathbf{V}$	Right and left stretch tensor
$\mathbf{R}$	Rotation tensor
$\mathbf{C} = \mathbf{U}^2 = \mathbf{F}^T\mathbf{F}, \mathbf{B} = \mathbf{V}^2 = \mathbf{F}\mathbf{F}^T$	Right and left Cauchy-Green tensor
$\mathbf{E} = \frac{1}{2}(\mathbf{C} - \mathbf{1})$	Green strain tensor
$I_i(\mathbf{B})$	Invariants of $\mathbf{B}$

$\lambda_i > 0$	Principal stretches
$\{\mathbf{l}_i\}$	Left principal basis
$\{\mathbf{r}_i\}$	Right principal basis
$\mathbf{T}$	Cauchy stress
$\mathbf{T}_R$	First Piola stress
$\mathbf{T}_{RR}$	Second Piola stress
σ_i	Principal value of Cauchy stress/true stress
s_i	Principal value of Piola stress/engineering stress/nominal stress
ρ_R	Mass density per unit reference volume
ψ_R	Free energy density per unit reference volume
b_{0R}	Body force per unit reference volume
p	Arbitrary pressure
μ	Generalized shear modulus
$\boldsymbol{\phi}_i$	Eigen modes

2.2 Characterization of material behavior

A silicone rubber (Elite Double 8, Zhermack) is used throughout this study. The major macroscopic physical characteristic of this material is its ability to sustain large reversible strains with negligible hysteresis, which makes it ideal to be modeled by the theory of finite elasticity. Uniaxial compression tests were conducted to determine the material constants.

A mold was made from acrylic sheets using laser cutting to cast the material testing specimen. The testing specimen was a cylinder with a radius of 10 mm and a height of 6.35 mm (Figure 2.1).

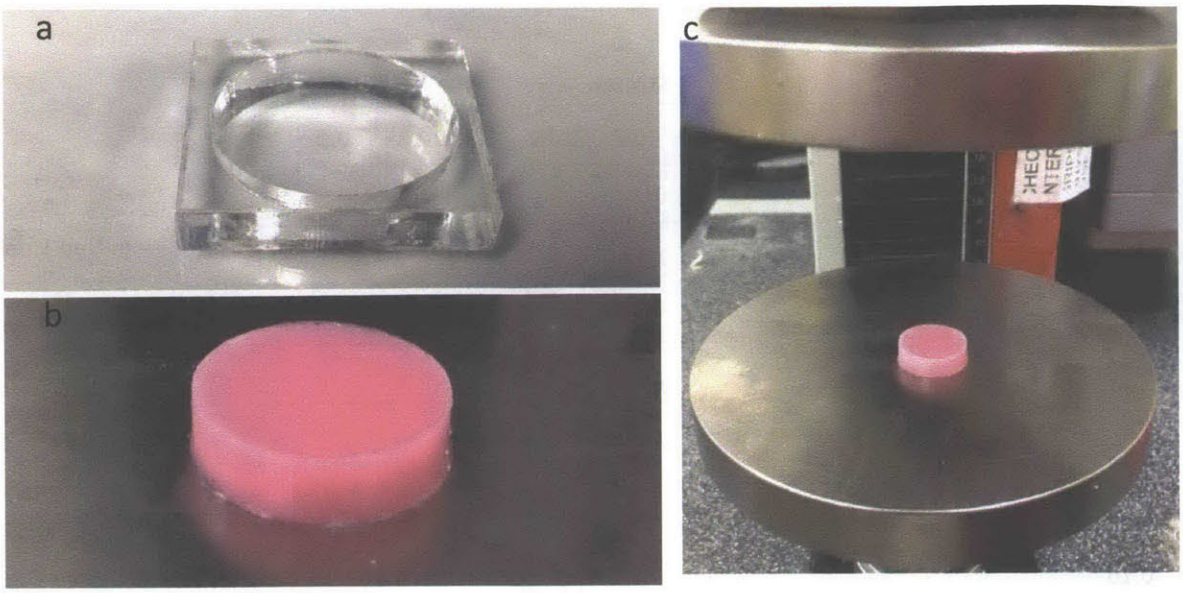

Figure 2.1 (a) Acrylic mold (b) Cylindrical testing specimen with a radius of 10 mm and a height of 6.35 mm (c) Uniaxial compression test setup

Uniaxial compression tests were conducted on the specimen to characterize the material response of the elastomeric matrix and the behavior was found to be well captured by a simple Neo-Hookean model. The specimen was subjected to uniaxial compression at different strain rate using a Zwick screw-driven testing machine. Vaseline was used to reduce the friction effects between the sample and the plates. The tests showed that the material exhibits a behavior typical for elastomers: large strain elastic behavior with negligible rate dependence and negligible hysteresis during a loading-unloading cycle. The material behavior at a compression speed of 20 mm/min is reported in Figure 2.2 and is used to determine the shear modulus.

The uniaxial stress-strain behavior of the material up to an applied strain of over 35% was found to be well captured using an incompressible Neo-Hookean model, whose strain energy is,

$$\psi = \frac{\mu_0}{2}(I_1 - 3) \tag{2.1}$$

where μ_0 is the initial shear modulus and I_1 is the first invariant of the left Cauchy Green tensor. This covers well beyond the range of strain in this study. After curve fitting, the initial shear modulus was found to be 0.058 MPa.

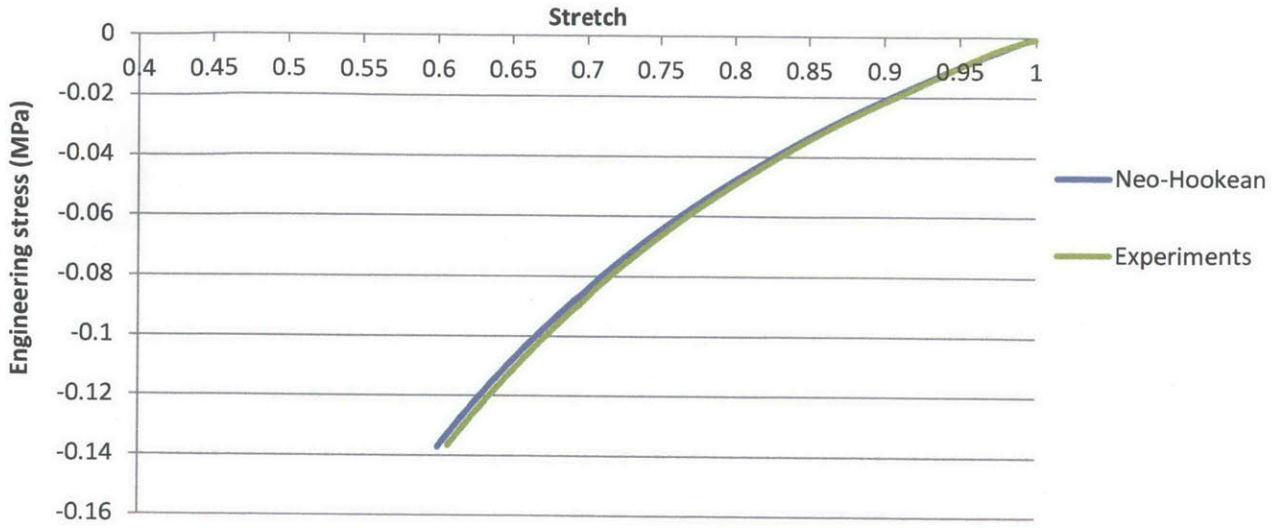

Figure 2.2 Engineering stress vs. principle stretch. Comparison between experiment and Neo-Hookean model

2.3 Boundary conditions for infinite periodic structures

When analyzing a structure with complicated and repeating units of microstructures, we often use periodic boundary conditions. One methodology was first developed by Danielsson, Parks and Boyce [1].

The key idea of this methodology is that instead of analyzing the entire structure, we consider a representative volume element (RVE) that contains one or multiple unit cells of the structure. A unit cell is defined as the smallest repeating geometric units. Figure 2.3 shows a structure with repeating units. Square ABCD is a unit cell; the unit cell itself is typically taken as the RVE. However, with deformation, instabilities may actually have their lowest energy mode over multiple "initial unit cells", hence changing the "unit cell" to require more of the "initial unit cells". Therefore, we also consider RVEs include multiple "initial unit cells" such as the square EFHG containing four unit cells. We impose boundary conditions on the RVE to capture the periodic nature of the deformation of the RVE edge boundaries, written in terms of the macroscopic deformation gradient and the local position of the edge nodes. Using periodic boundary conditions is not only computationally efficient but also eliminates the artificial boundary effects of the finite structure.

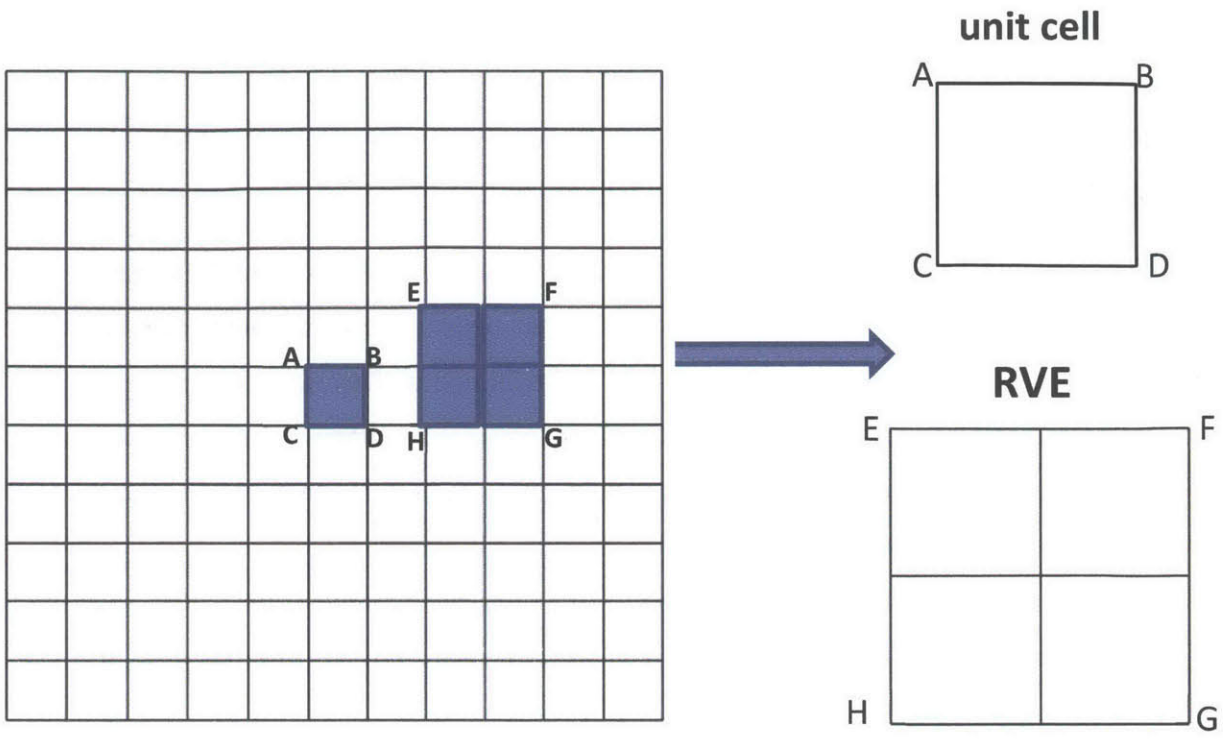

Figure 2.3 A periodic structure and its corresponding unit cell and RVE

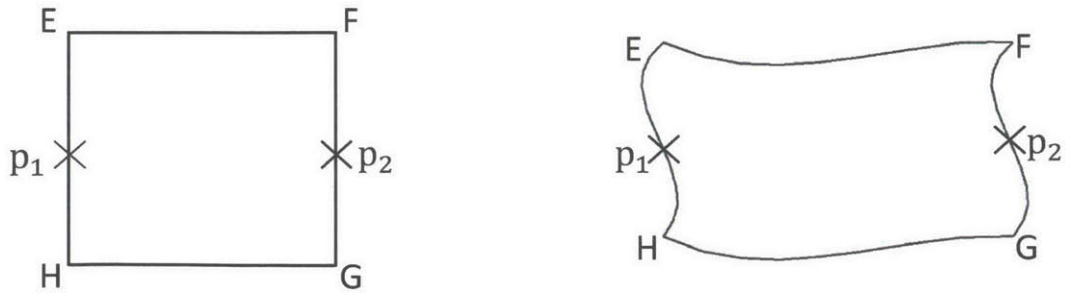

Figure 2.4 A RVE deforming under periodic boundary conditions with p_1 and p_2 periodically located on the RVE boundary

The periodic boundary condition can be mathematically defined as follows:

$$\mathbf{u}_{p_2} - \mathbf{u}_{p_1} = \mathbf{H}(\mathbf{X}_{p_2} - \mathbf{X}_{p_1}) = (\mathbf{F} - \mathbf{1})(\mathbf{X}_{p_2} - \mathbf{X}_{p_1}) \tag{2.2}$$

where p_1 and p_2 are two points periodically located on the RVE boundary, shown in Figure 2.4. **F** denotes the macroscopic applied deformation gradient.

To implement in finite element programs, we impose the macroscopic deformation by prescribing the components of **H** through a set of virtual nodes. The components of **H** are assigned to be the displacement components of the virtual nodes. Therefore, by prescribing corresponding displacements of the virtual nodes, we can realize different macroscopic loading conditions including uniaxial compression, biaxial tension and simple shear. Using the principle of virtual power, the components of the macroscopic first Piola stress **S** are identified as the reaction forces of the virtual nodes divided by V_0, the reference volume of the RVE. Then the Cauchy stress can be found through $\mathbf{T} = \frac{V_0}{V}\mathbf{S}\mathbf{F}^T$, where V is the volume of the deformed configuration. The components of the macroscopic nominal strain are simply equal to the displacements of the virtual nodes.

2.4 Eigen analysis

In this study, we mostly focused on infinite periodic structures for the sake of computational efficiency with a few analyses performed on finite-sized specimens to enable comparison with the experimental results.

The stability of both the finite-sized specimens and the corresponding infinite periodic structures was first examined using eigenvalue analysis. It is a linear perturbation procedure that perturbs an arbitrary reference load by λ and seeks alternative configurations that can sustain the perturbed load [2], [3]. It is essentially an eigenvalue problem. In our study, this procedure was implemented using the *BUCKLE module in the commercial finite element package ABAQUS/Standard. It returns an eigenmode which corresponds to a buckled shape and an eigenvalue which corresponds to a critical stress/strain. There can be multiple eigenvalues and eigenmodes.

It is rather straightforward for a finite-sized specimen. However for its infinite periodic counterpart a Refined Eigen Analysis [4], [5] is needed because it is possible that there exists a microscopic bifurcation with a longer periodic length than a "unit cell." A "unit cell" here is defined as the smallest repeating geometry unit. Therefore, in order to obtain the correct eigenvalue and eigenmode of an infinite periodic structure, we should perform eigenvalue analysis on RVEs with an increasing number of unit cells. Then the critical load of the infinite periodic structure is defined as the infimum of the critical load on all possible RVEs. This approach is referred to as Refined Eigen Analysis.

In particular, an RVE is constructed consisting of **p**Y cells, where $\mathbf{p} = (p_1, p_2)$ and Y serves as a unit cell. Periodic boundary conditions described in Section 2.2 were imposed and linear buckling analysis was performed on each RVE with increasing **p**. In theory, we need to examine an infinite number of RVEs for different values of **p,** but for practical purposes, RVE size up to 10Y by 10Y is sufficient to get a reasonable understanding of material behaviors.

2.5 Post-buckling analysis

The eigenvalue analysis using *BUCKLE in ABAQUS is a one-step linear analysis that only returns the end-state data, i.e., eigenvalues and eigenmodes. It does not provide any information about the material response prior to or after the bifurcation. On the other hand, a static analysis using *STATIC in ABAQUS does generate progressive data at each time increment, but it does not capture the bifurcation at the critical load. In order to depict both the buckling and evolution of material behavior, we introduce an imperfection in the form of the first buckling mode $\boldsymbol{\phi}_1$(the eigenmode with the lowest eigenvalue) obtained from the linear buckling analysis to perturb the mesh by a small amount, scaled by a scale factor w,

$$\Delta \mathbf{x}_0 = w \frac{d_x + d_y}{2} \boldsymbol{\phi}_1 \tag{2.7}$$

Thus, the perturbation $\Delta \mathbf{x}_0$ introduced into the mesh is a fraction of the average center-to-center distance between the voids (d_x and d_y denoting the horizontal and vertical center to center distance, respectively). With this initial imperfection, the structure can capture the bifurcation point during a static analysis and deform as the first buckling mode.

2.6 References

[1] M. Danielsson, D. M. Parks, and M. C. Boyce, "Three-dimensional micromechanical modeling of voided polymeric materials," J. Mech. Phys. Solids, vol. 50, no. 2, pp. 351–379, Feb. 2002.

[2] R. D. Cook, M. E. Plesha, D. S. Malkus, and R. J. Witt, "Concepts and applications of finite element analysis," 2002.

[3] S. Timoshenko, Theory of Elastic Stability. McGraw-Hill Book Company, Incorporated, 1936, p. 518.

[4] K. Bertoldi, M. C. Boyce, S. Deschanel, S. M. Prange, and T. Mullin, "Mechanics of deformation-triggered pattern transformations and superelastic behavior in periodic elastomeric structures," J. Mech. Phys. Solids, vol. 56, no. 8, pp. 2642–2668, 2008.

[5] G. Geymonat, S. Muller, and N. Triantafyllidis, "Homogenization of nonlinearly elastic materials, microscopic bifurcation and macroscopic loss of rank-one convexity," Arch. Ration. Mech. Anal., vol. 122, no. 3, pp. 231–290, 1993.

Chapter 3
Pattern transformation of periodic elastomeric structures with a square array of circular holes

Before introducing our key design features (the contact nubs and the conduction pathways), it is worthwhile to extend some of the key results of the modeling of an elastomeric periodic matrix with circular holes on a square lattice, especially the effect of void-volume fraction on critical stress, as they provide important guidance for our design. This section essentially follows the approach by Bertoldi and Boyce [1].

3.1 Infinite periodic structure, unit cell and RVE

As was briefly mentioned in Section 2.3, we analyze infinite periodic structures for computational efficiency. Figure 3.1(a) shows an infinite periodic structure with circular holes. A unit cell is defined as the smallest repeating geometric unit of the periodic structure, as is shown in Figure 3.1(b). A representative volume element (RVE) contains m × m repeating unit cells. Figure 3.1 (c)-(e) show RVEs of size 2 × 2, 3 × 3 and 4 × 4.

Since the infinite periodic structure is just the repeating of the unit cells, the void-volume fraction ψ of the infinite structure can thus be defined as

$$\psi = \frac{\pi R^2}{L^2} \tag{3.1}$$

where R is the radius of the circular void and L is the length of the unit cell square shown in Figure 3.1(b). To examine specimens with various void-volume fractions, we can simply change the ratio between R and L.

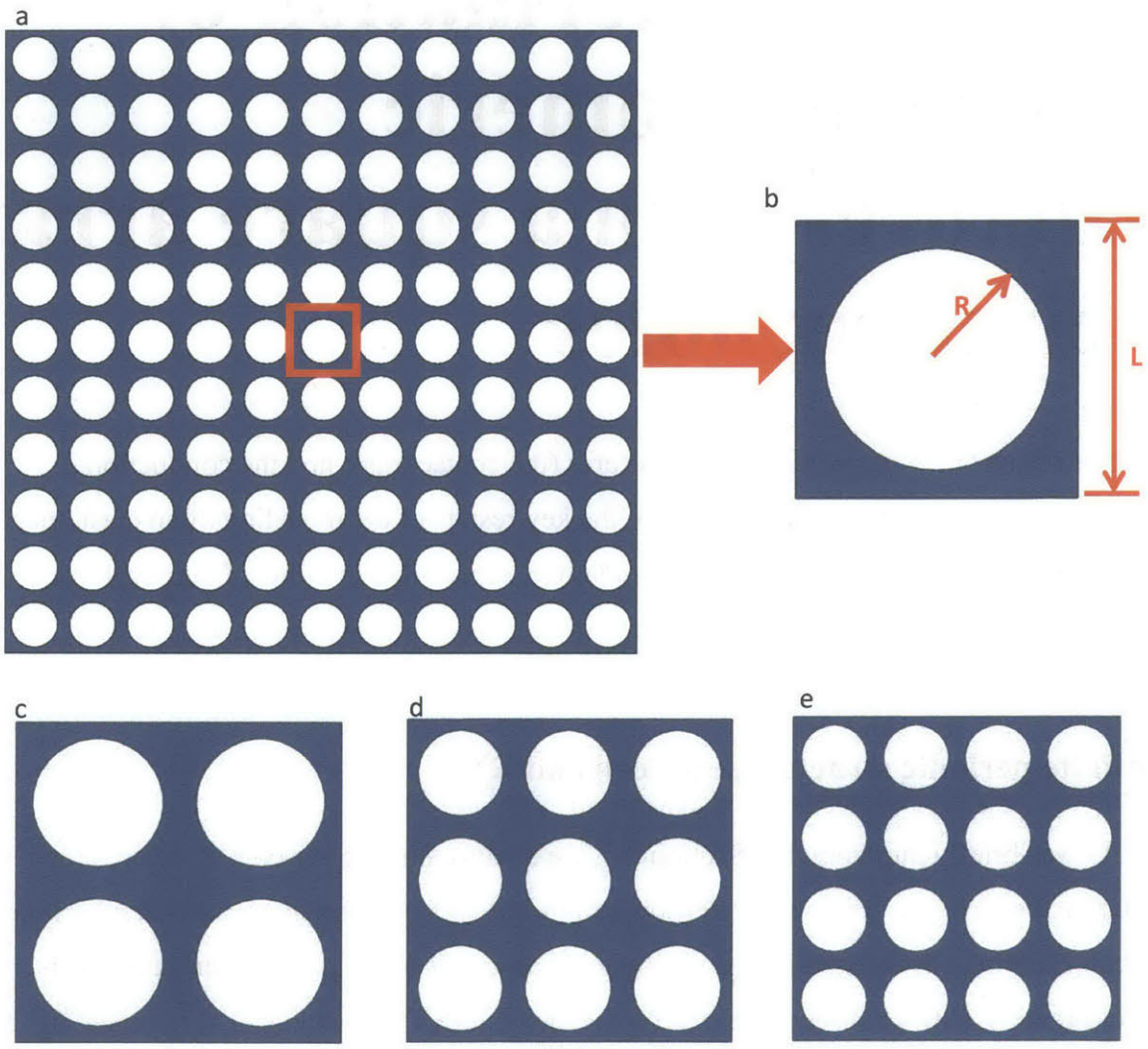

Figure 3.1 (a) An infinite periodic structure with circular holes (b) Corresponding unit cell (c) Corresponding 2 × 2 RVE (d) Corresponding 3 × 3 RVE (e) Corresponding 4 × 4 RVE

3.2 Analysis of instability

We analyzed three void-volume fractions $\psi = 30\%, 50\%$ and 60%. Figure 3.2 shows the infinite periodic structures and the corresponding unit cells.

Following the procedure by Bertoldi and Boyce [1], Refined Eigen Analysis (Section 2.4) was performed on RVEs consisting of m × m (m = 2,3, ... ,10) unit cells for all three void-volume fractions, a total of 27 RVEs. All analyses were performed in ABAQUS/Standard using *BUCKLE module. The material model used was the Neo-Hookean model (Section 2.2) with a shear modulus of 0.058MPa. Infinite periodic boundary conditions (Section 2.3) with uniaxial loading were imposed. Triangular, quadratic plane strain elements (CPE6H) were used.

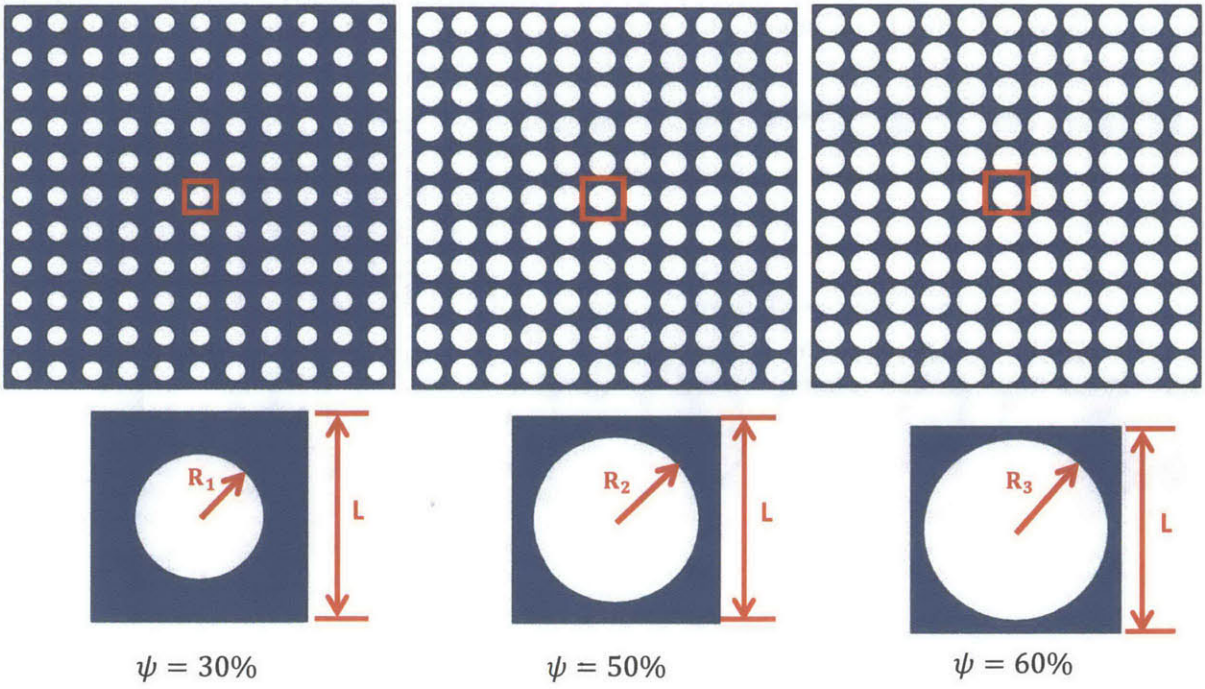

Figure 3.2 Infinite periodic structures and their corresponding unit cells with void-volume fraction $\psi = 30\%, 50\%$ and 60%

Figure 3.3 shows the first and second mode of $\psi = 50\%$ for cases where $\mathbf{p} = (2,2)$, $\mathbf{p} = (3,3)$, $\mathbf{p} = (4,4)$, $\mathbf{p} = (5,5)$ and $\mathbf{p} = (6,6)$. $\psi = 30\%$ and $\psi = 60\%$ showed similar modes.

The figure clearly shows that eigenmodes of the RVE vary with the number of unit cells it consists of. Interestingly, the same first eigenmode exists for RVEs that consist of even number of unit cells (i.e. $\mathbf{p} = (2n, 2n), n = 1,2 \ldots$). In other words, the first mode of a 6×6 RVE can be assembled by three 2×2 RVEs. This does not hold for either the second mode or the odd-sized RVEs. This observation suggests that the first mode of the even-sized RVEs is a result of local instability that occurs through the entire structure, causing the global periodic pattern transformation. Higher modes are not presented here as they are unlikely to occur due to their high critical loads. However, one may preferentially activate high modes by placing inclusions in the voids. This is yet beyond the scope of this study and thus will not be discussed.

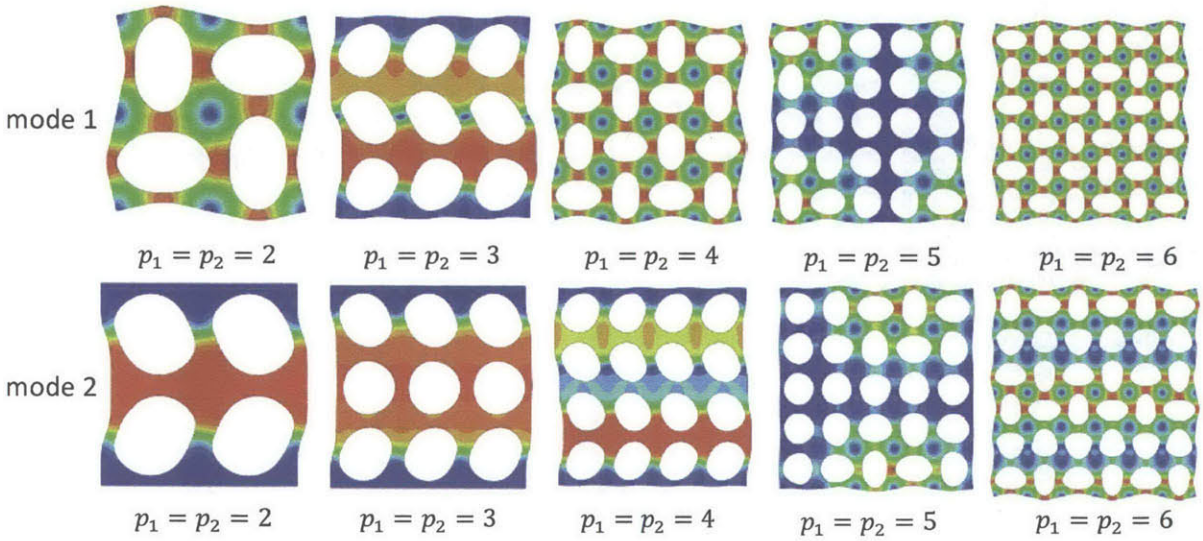

Figure 3.3 First and second eigenmode for $\psi = 50\%$ for $\mathbf{p} = (2,2)$, $\mathbf{p} = (3,3)$, $\mathbf{p} = (4,4)$, $\mathbf{p} = (5,5)$ and $\mathbf{p} = (6,6)$

To quantitatively verify the above observation, we plot the eigenvalues against RVE size in Figure 3.4. As is clearly shown in the plot, even-sized RVEs have the same values for the lowest critical load and hence are the preferred eigen modes. This indicates a repeating 2X2 first buckling mode throughout the structure.

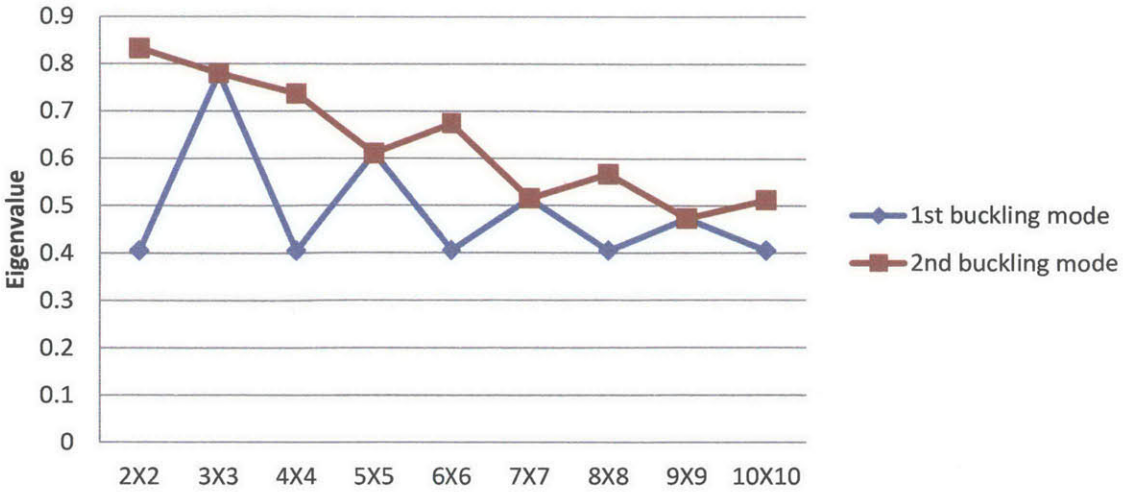

Figure 3.4 Eigenvalue vs. RVE size for $\psi = 50\%$. $\psi = 30\%$ and $\psi = 60\%$ showed similar trends with different eigenvalues.

3.3 Post-buckling analysis

From the Refined Eigen Analysis in the previous section, a 2×2 RVE was used for post-buckling analysis to obtain stress-strain data for post-buckling behavior. An imperfection in the form of the first buckling mode was introduced to preferentially activate the first mode. Figure 3.5 shows the stress-strain curve for each void-volume fraction.

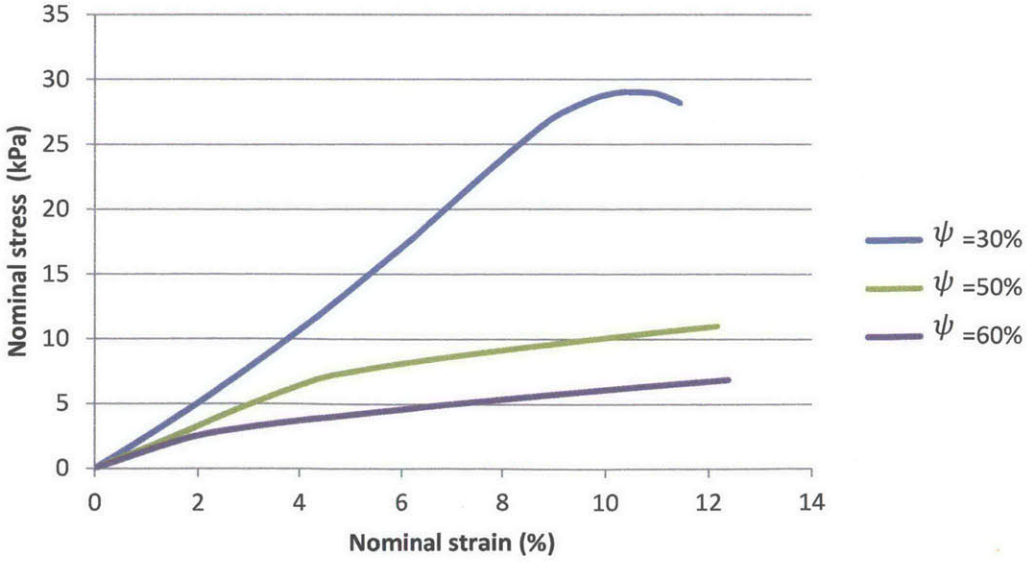

Figure 3.5 Nominal strain vs. nominal stress for $\psi = 30\%$, $\psi = 50\%$ and $\psi = 60\%$

From the plot, we can see that:

(1) All three curves have three distinct regimes: a linear elastic response followed by a distinct rollover at a critical load followed by a much reduced slope (a near plateau like regime) This is clearly a result of the buckling at the critical load.

(2) Although all structures exhibited similar behaviors, a departure from linearity due to instability, their critical stress or critical strain at buckling were quite distinct.

3.4 Understanding the effect of void-volume fraction

The observations in Section 3.3 can be conceptually understood as follows.

The ligaments between the voids can be viewed as small beam elements. Figure 3.6 shows a beam subject to compressive load and the first buckling mode of the beam when the load reaches a critical value.

From Euler beam buckling, the critical load for beam buckling with pinned-pinned ends is

$$P_{cr} = EI(\frac{n\pi}{L})^2 \tag{3.2}$$

where E is the Young's modulus, I is the moment of inertia and L is the beam length.

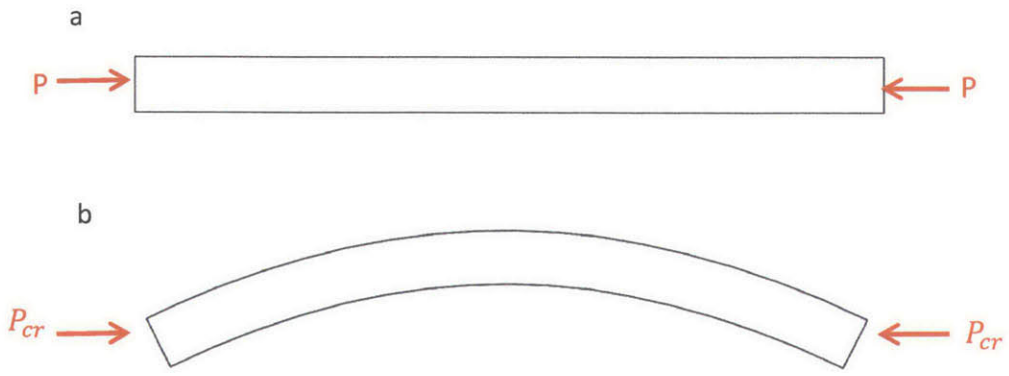

Figure 3.6 (a) A beam subject to compressive load (b) The first buckling mode of the beam when the load reaches a critical value.

Figure 3.7 shows the dimension of the beam with Young's modulus E. Let the symbol "~" denote "proportional to" or "scale as" and we conduct the following scaling

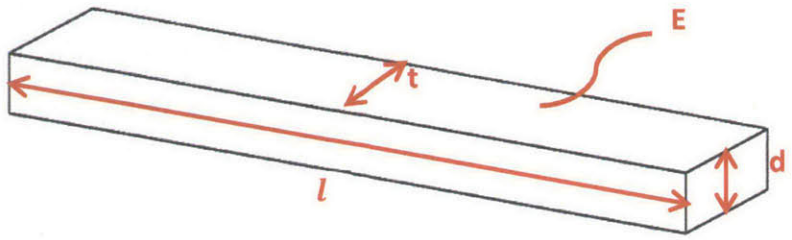

Figure 3.7 Dimensions of the beam

The moment of inertia I is scaled as

$$I \sim d^3 t \tag{3.3}$$

where d is the in-plane width of the beam and t is the depth.

Thus, the critical force is scaled as

$$P_{cr} \sim \frac{I}{l^2} \sim \frac{d^3 t}{l^2} \tag{3.4}$$

where L is the in-plane length of the beam.

Then, the cross-sectional area is scaled as

$$A \sim dt \tag{3.5}$$

Hence, the critical stress

$$\sigma_{cr} = \frac{P_{cr}}{A} \sim \frac{P_{cr}}{dt} \sim \frac{\frac{d^3 t}{l^2}}{dt} = \left(\frac{d}{l}\right)^2 \tag{3.6}$$

The term d/l is usually referred to as the slenderness ratio of the beam. As we can see, the critical buckling stress is proportional to the slenderness ratio of the beam squared, meaning the more slender the beam, the lower the critical stress it takes to buckle.

We apply this result to the understanding of the behavior of our periodic cellular structures. The internal ligaments between the voids can be modeled as beam elements. The effective beam length l can be approximated as the diameter of the void, while the effective beam width d can be approximated as the smallest distance between the voids. Hence, the slenderness ratio of the ligament is also d/l. l and d are depicted in Figure 3.8 (a). Moreover, the relation between the critical stress of the local ligament and the macroscopic critical stress is depicted in Figure 3.8(b). The critical stress of the local ligament is the critical stress we described above in the beam analogy. It should be proportional to the slenderness ratio of the ligament.

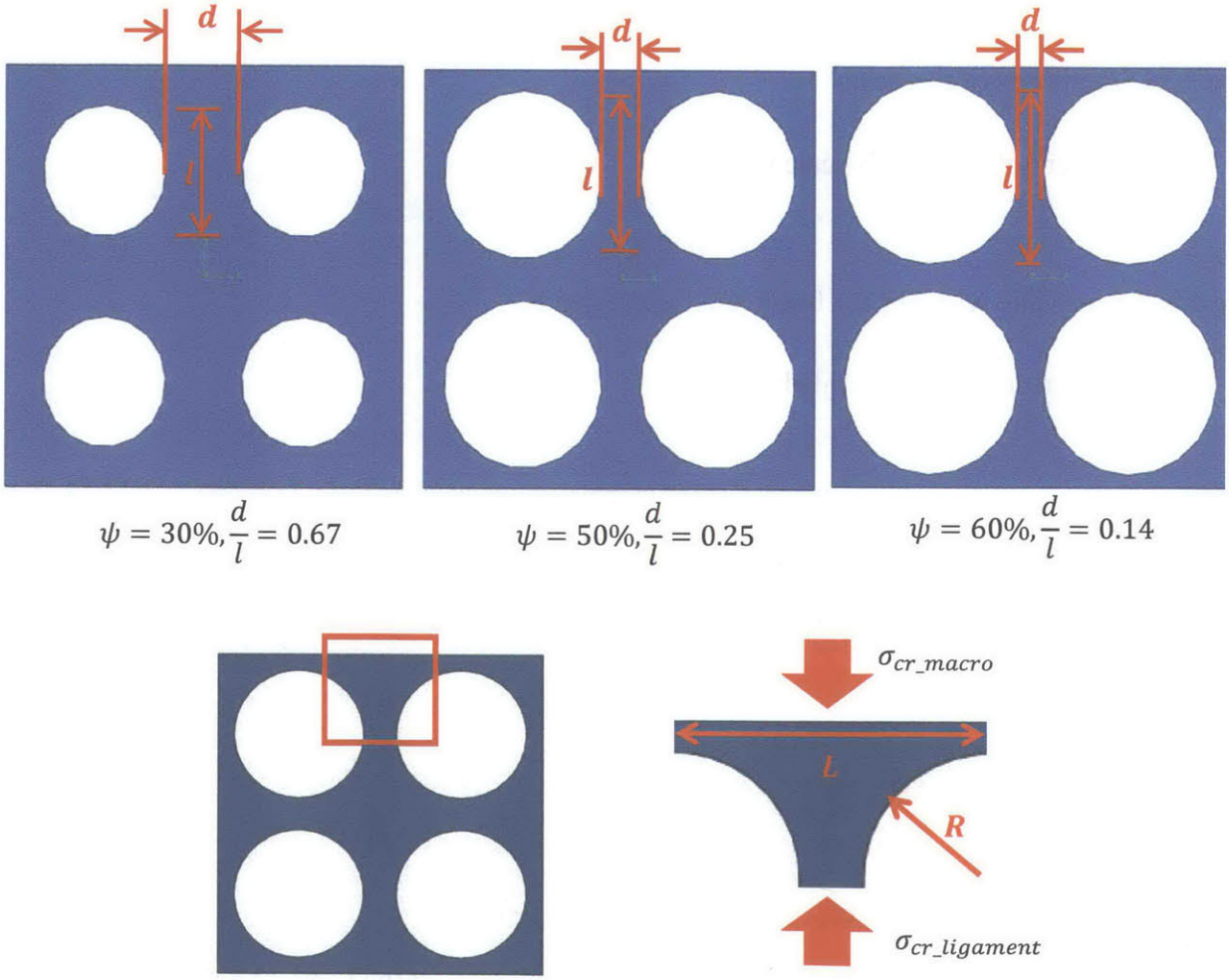

Figure 3.8 (a) Inter-void ligament slenderness of RVE with different void volume fractions (b) relation between critical stress of the ligament and the macroscopic critical stress

When the whole structure is compressed, the ligaments experience mainly the compressive load along their l direction. When the local compressive stress is below the critical value, the ligament behaves linearly as a normal linear elastic column, which explains the linear regime of the stress-strain curve. However, as the deformation becomes larger, the local compressive stress reaches the critical value and thus all the ligaments buckle in a way similar to Euler beam buckling. This accounts for the critical stress followed by the stress plateau after the linearity.

To quantitatively look into the effect of the slenderness ratio of the ligament, we plot $\sigma_{cr\_ligament}$ vs. $\frac{d}{L}$ in Figure 3.9. The values of $\left(\frac{d}{L}\right)$ and $\sigma_{cr\_ligament}$ are normalized by their values at $\psi = 60\%$.

The void-volume fraction is related by the ratio of d/l and the macroscopic critical stress is related to the local ligament critical stress; therefore if we plot the macroscopic critical stress vs. void-volume fraction, it follows the same trend as local ligament critical stress vs. slenderness ratio. This is shown in Figure 3.10.

It can be clearly seen from Figure 3.8 that the inter-void ligament of $\psi = 60\%$ is much longer and thinner than that of $\psi = 30\%$, or equivalently has a larger slenderness ratio, so it should buckle much earlier than $\psi = 30\%$ and have a lower local and macroscopic critical stress. This conclusion is in good agreement with the stress-strain plot in Figure 3.5.

It is worth noting that critical stress is strongly affected by the void-volume fraction or the slenderness ratio, as is shown in Figure 3.9 and Figure 3.10. The macroscopic critical stress drops by nearly 70% when the void-volume fraction increases from 30% to 50%. This makes a huge difference in designing deformation-induced devices as will be explained in the following chapters.

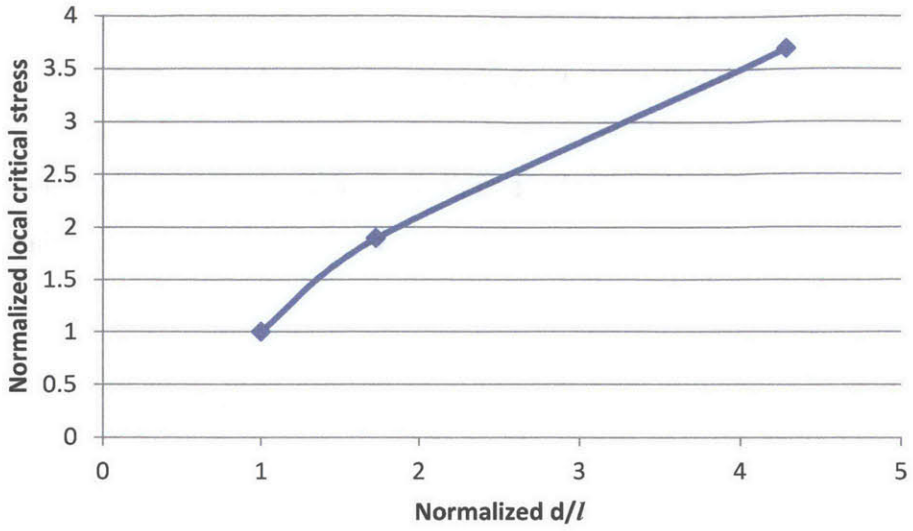

Figure 3.9 normalized $\sigma_{cr\_ligament}$ vs. d/l

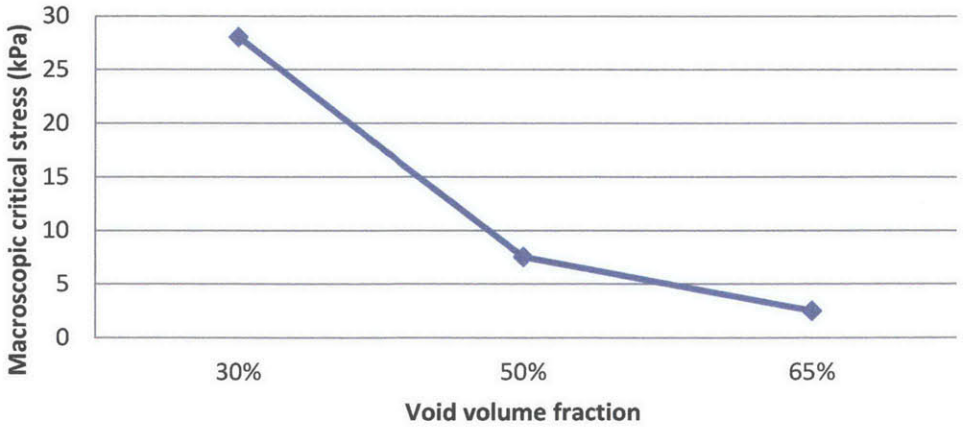

Figure 3.10 Void-volume fraction vs. critical stress

3.5 Conclusions

Here, we summarize the important results from analyzing circular holes on a square lattice of varying void-volume fraction, as they are crucial to our design in the following chapters.

(1) An elastomeric periodic cellular structure comprising of square arrays of circular holes would suddenly transform into a periodic pattern of alternating and mutually orthogonal

ellipses (Figure 3.2) upon reaching a critical load. This dramatic shape change offers the opportunity for the design of tunable and deformation-controlled switches.

(2) The global dramatic pattern transformation is a result of the buckling of the inter-void ligaments.

(3) The void-volume fraction has a strong effect on the onset of buckling (i.e. critical stress and strain).

3.6 References

[1] K. Bertoldi, M. C. Boyce, S. Deschanel, S. M. Prange, and T. Mullin, "Mechanics of deformation-triggered pattern transformations and superelastic behavior in periodic elastomeric structures," J. Mech. Phys. Solids, vol. 56, no. 8, pp. 2642–2668, 2008.

Chapter 4
Micromechanical model based design of contact nubs

In this chapter, in order to make connections within the voids upon pattern transformation, we introduce a microstructural feature – contact nubs. It is reasonable to expect the response of the structure with nubs will be different from the one without the nubs due to the change in the microscopic structure. Therefore, to explore the effect of adding contact nubs on the structural behavior, finite element models were built and analyzed in the commercial finite element package ABAQUS. A series parametrical analysis was undertaken over different nub geometrical parameters to test and optimize the nub geometry. The input file for ABAQUS was generated using MATLAB scripts.

In the following sections, the finite element model used, the nub design parameters and the simulation results are presented.

4.1 Conceptual design

In light of the conclusions drawn from Chapter 3, the periodic structure showed great potential for the design of instability-induced switches and yet one major challenge remains; how to utilize the dramatic shape change upon buckling. In this section, we present a novel design feature, which we refer to as the "contact nubs" to take advantage of the shape transformation of voids from circle to ellipse.

The difference between a circle and an ellipse is that an ellipse has one long major axis and one short minor axis while a circle has essentially an infinite number of pairs of "major" and "minor" axes of the same length. The design idea is simple, as shown in Figure 4.1. By adding a pair of nubs, we make the connection when the circular void on the left buckles into an elliptical void on the right, turning the sudden shape change into a real "switch".

Particularly, when the load is below the critical load, even though the circle is compressed, the deformation is still relatively small so that the nubs are not in contact, which means the switch is off. Only if the load and the strain pass the critical value, the circular void would suddenly transform into the elliptical shape so that contact between the nubs is then initiated, which means the switch is on. Since the material is elastic, this process can be repeated. Therefore, a switch that can be turned on and off via deformation is realized.

We also note that since the void shape is symmetric, we can add two pairs of nubs aligned vertically and horizontally, so that at least one pair of nubs can make contact regardless of the loading direction.

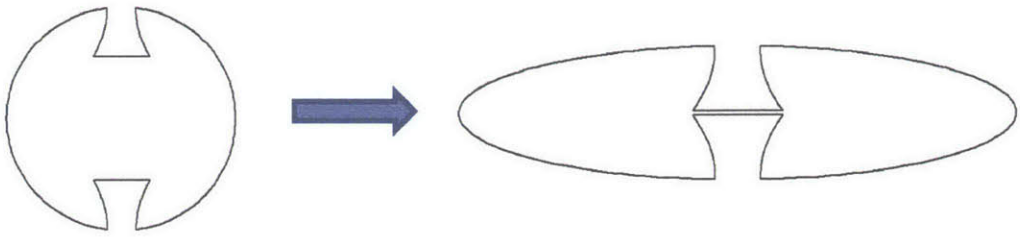

Figure 4.1 The conceptual design of contact nubs

4.2 Design parameters

The nub design concept is easy to grasp, however, adding nubs is essentially changing the microstructure of the periodic structure. It presumably could affect the instability response of the structure. Therefore, the effect of nub geometry on the buckling and post-buckling behavior of the structure needs further investigation.

Guided by engineering intuition, we identified three major geometrical parameters as shown in Figure 4.2.

A is the length of intersection between the nub and the inter-void ligament. B is the width of the nub end that makes the contact. C is the distance between the opposing nubs. Therefore, A is used to examine the effect of the connection between the nubs and the inter-void ligament. B is used to examine the contact between the mating nubs. C is used to examine the strain level at which the nubs make contact. A larger C means that greater strain or stress is required to achieve

contact. We also looked into the effect of all three parameters and their relationship with the void-volume fraction. The results are reported in the next few sections.

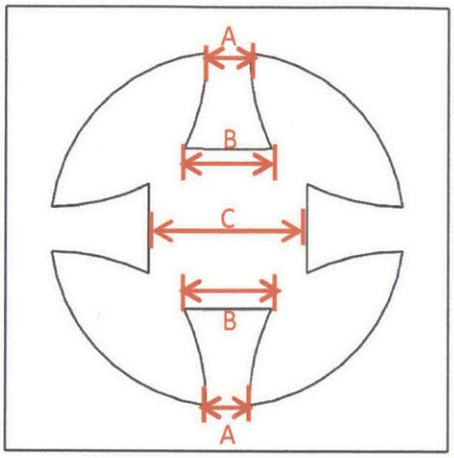

Figure 4.2 Nub design parameters

4.3 Effect of nub geometries for fixed void-volume fractions

From Chapter 3, we know that the critical load is strongly dependent on the void-volume fraction. Here, in order to examine solely the effec of nub geometry, we kept the void-volume fraction $\psi = 50\%$ fixed and varied the parameters A, B and C. The focus here is still the eigenvalues and eigenmodes, or in other words, critical stress and strain.

4.3.1 Keep A constant while varying B and C

We still used 2x2 RVEs as we assume that there would be the same 2x2 periodicity as in the structures without the nubs. A total of nine structures were considered (see Figure 4.3). We normalized the parameters by R to make our studies applicable to different length scales.

The first buckling mode essentially follows that of the structure without the nubs; however, the eigenvalues are changed quite a bit due to the effect of the additional "nub" material at the beam center which also aids in resisting buckling. Figure 4.4 shows the first mode of the specimen with $A = 0.25R, B = 0.5R, C = 0.6R$. The nubs make connections after the structure buckles as expected.

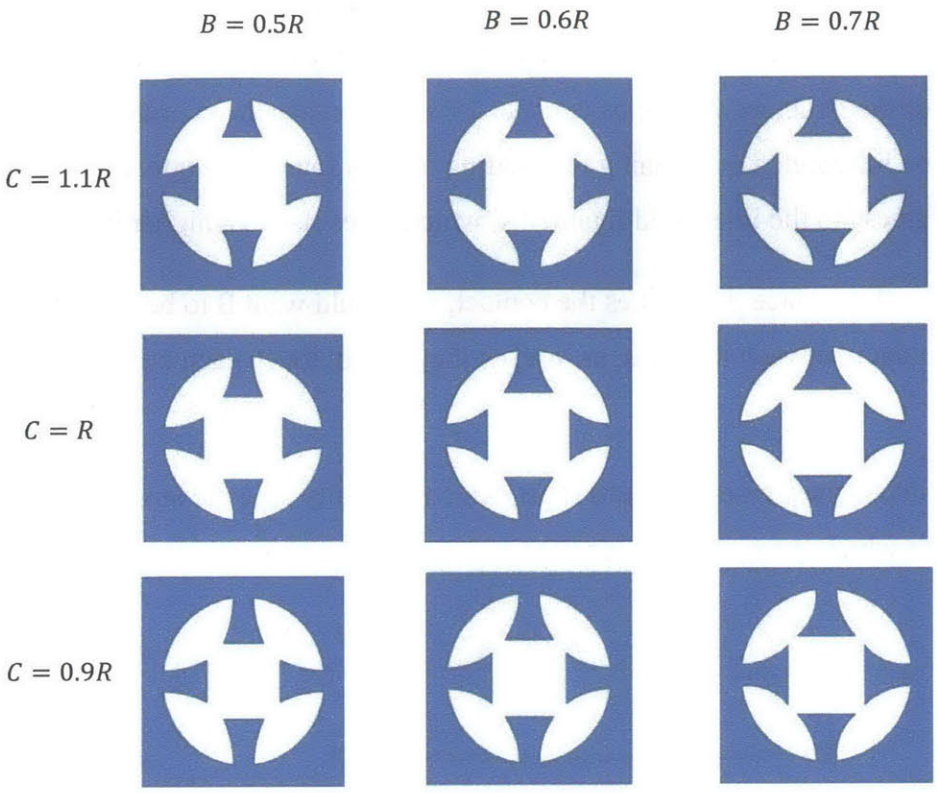

Figure 4.3 Nub shapes with B = 0.5R: 0.1R: 0.7R, and C = 0.9R: 0.1R: 1.1R while keeping A = 0.25R fixed

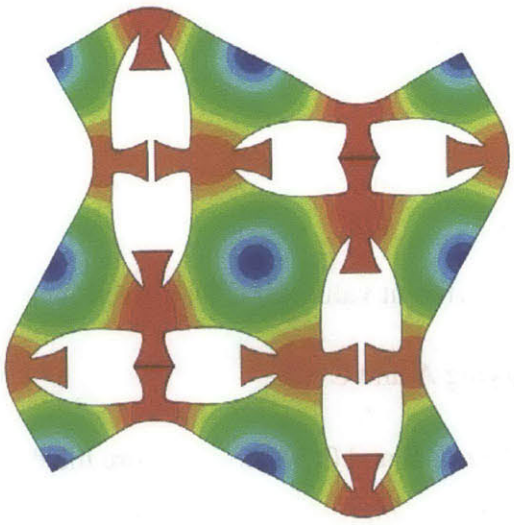

Figure 4.4 First mode of the specimen with Nub shapes with A = 0.25R, B = 0.5R, C = 0.6R

Eigenvalues plotted against B with different values C are shown in Figure 4.5. As we can see, there is no significant difference between different values of B or C for a fixed A. However, the eigenvalue of the structure with nubs is about 10% higher than those of the structures without nubs. This can be interpreted as meaning that adding nubs is somehow equivalent to adding more material and stiffness to the inter-void ligaments, which gives rise to a higher buckling load.

Since B is the surface that makes the contact, we would want B to be as large as possible to ensure full contact between the nubs, as long as they do not touch each other during the process.

Since C determines when the nubs meet, we could easily tune the length of C to control the strain level at which the nubs make contact.

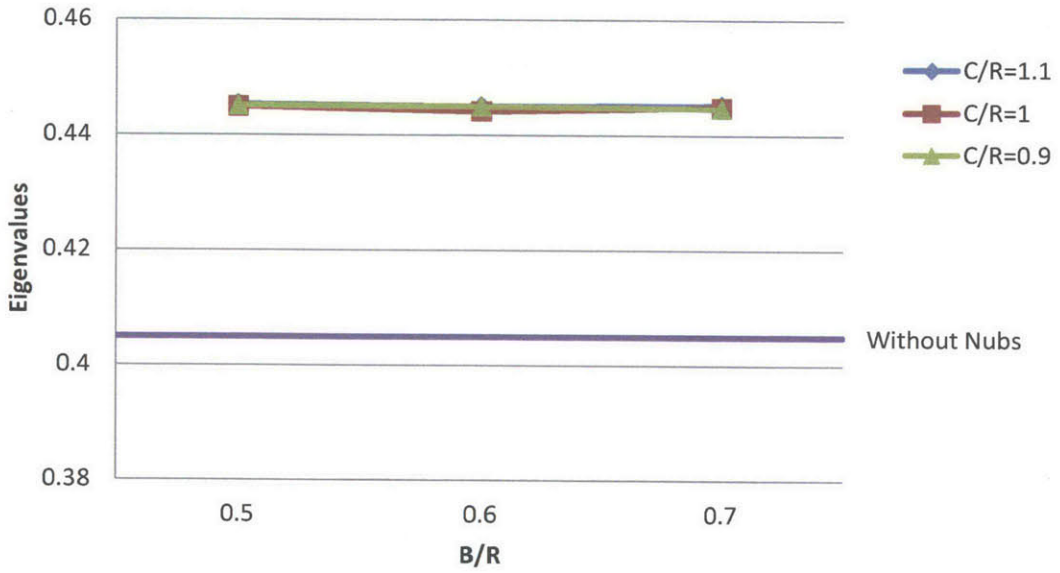

Figure 4.5 Eigenvalues vs. B for different values of C for a fixed A=0.25R

4.3.2 Keep B constant while varying A and C

Having identified the effect of B and C, we now explore the design parameter A that relates the nub with the ligaments, through Refined Eigen Analysis of the 2x2 RVEs. A total of nine structures were considered in this section (see Figure 4.6).

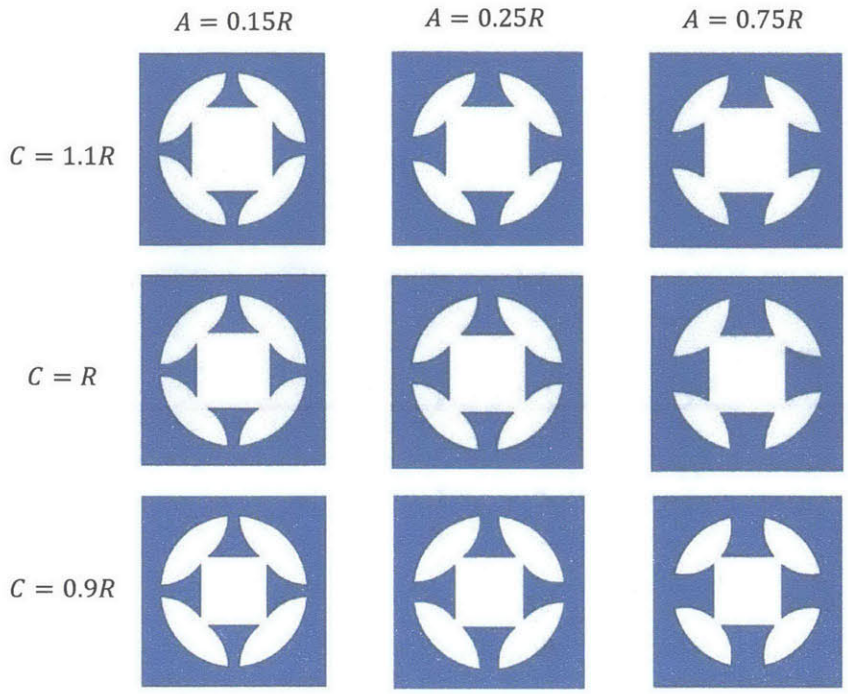

Figure 4.6 Nub shapes with C=0.9R, R, 1.1R, and A=0.15R, 0.25R, 0.75R, while keep B=0.7R fixed

The results are shown in Figure 4.7. As predicted in Section 4.3.1, the parameter C plays no role in determining the critical stress. However, parameter A, on the other hand, has a strong effect on the buckling load. The eigenvalue increases by nearly 30% as A increases from 0.15R to 0.75R.

This gives us great flexibility for designing our structures. For example, we can control the width of A to obtain the desired critical stress, or vice versa. Also, the strain level at which the nubs make contact is solely determined by C. Therefore, by simply adjusting the distance C between the nubs, we could easily control the contact strain.

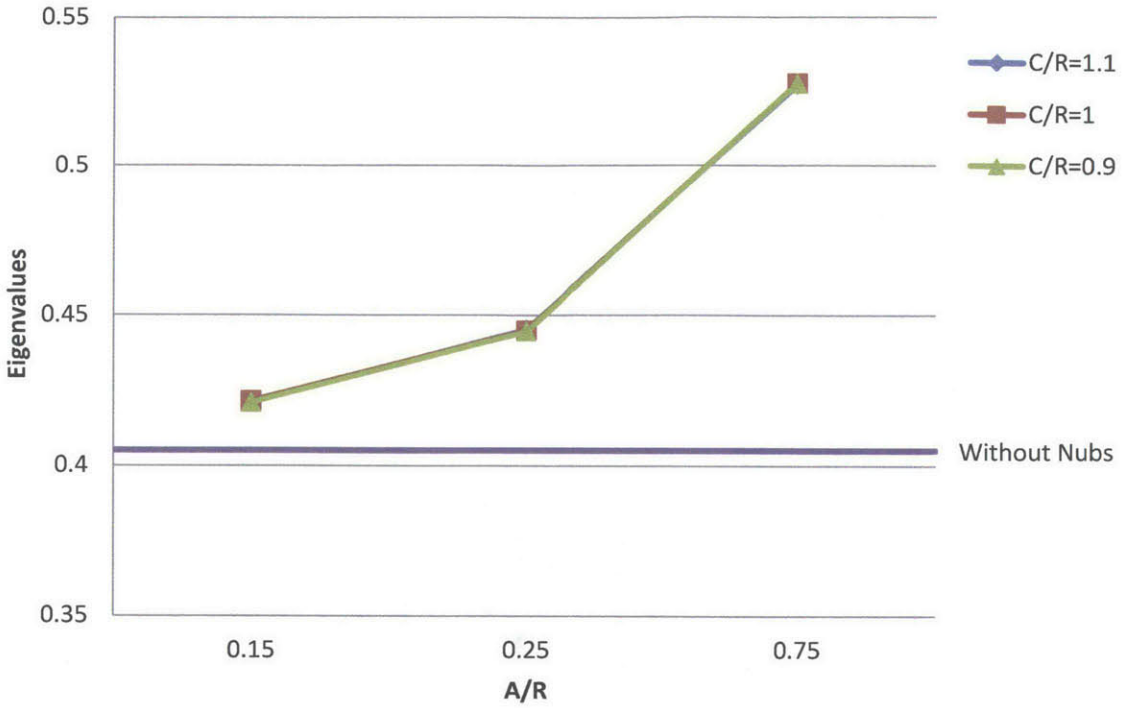

Figure 4.7 eigenvalues vs A for different values of C

4.4 Effect of void-volume fractions for fixed nub geometries

So far, we have examined the effect of nub geometry on material behavior at a given void-volume fraction. In this section, we evaluate the material response for a given nub geometry with the change of void-volume fraction. Three specimens with $\psi = 20\%, 50\%, 70\%$ were studied (see Figure 4.8). The nub geometry is the same for all three specimens with $A = 0.25R, B = 0.5R, C = 0.9R$.

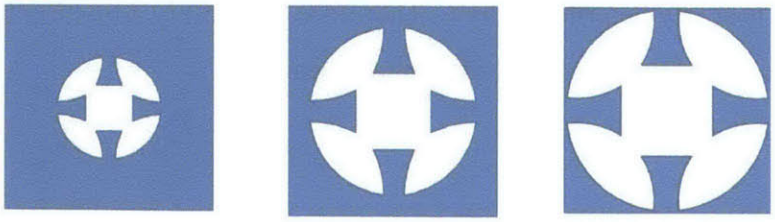

Figure 4.8 The 2D unit cell with $\psi = 20\%, 50\%, 70\%$. Nub design parameters are $A = 0.25R, B = 0.5R, C = 0.9R$.

We compare the results with structures without nubs in Figure 4.9. The eigenvalues of all three structures are larger than their corresponding structures without the nubs. However, the increase of eigenvalue is tremendously larger for structures with a small void-volume fraction.

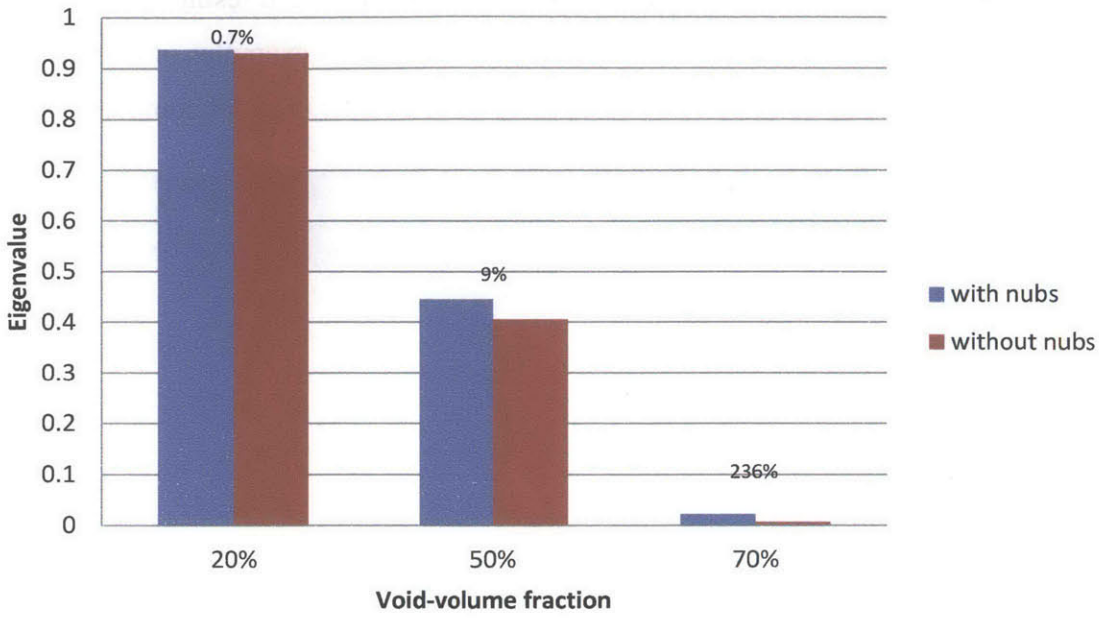

Figure 4.9 Comparison of eigenvalues between structures with and without nubs

4.5 Design of contact nubs for circular holes on a hexagonal lattice

Previous sections explored the design of contact nubs utilizing the alternating, mutually orthogonal elliptical pattern of an elastomeric matrix with a square array of circular voids after buckling. It has also been found that different hole arrangements would result in different buckling patterns for porous elastomers [1], [2]. Figure 4.10 shows examples of two distinct buckling patterns resulting from different hole arrangements under uniaxial compression.

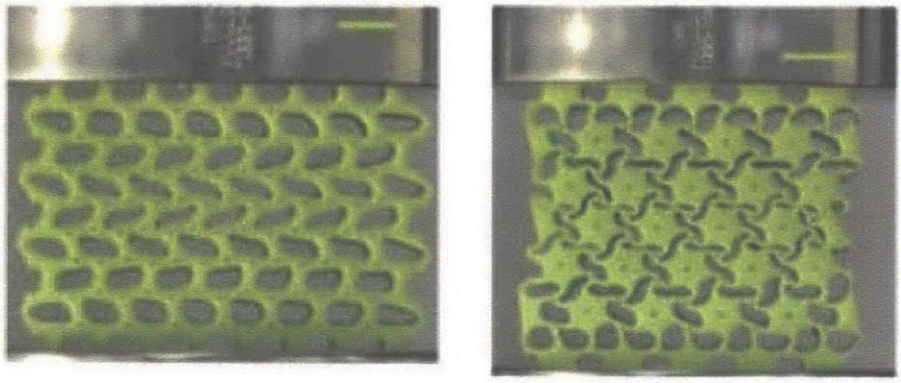

Figure 4.10 Two elastomeric porous structures with different hole arrangements buckle under uniaxial compression (Taken from Shim, Shan et al. 2013 [2])

The findings create more options for the design of our contact nubs, as the nubs do not necessarily need to be aligned vertically or horizontally. Their orientation can be tailored according to the buckling pattern.

Guided by the results in previous sections, we choose a nub design with $A = 0.25R, B = 0.5R, C = 0.9R$ and the void-volume fraction is $\psi = 50\%$. In this case, we simulated both a finite-sized specimen and its infinite periodic counterpart.

Figure 4.11 (a) shows a finite-sized sample with a 7X8 hexagonal array of circular holes with nubs while Figure 4.11 (b) shows a RVE representing its infinite periodic counterpart.

Note that the RVE was deliberately chosen as in Figure 4.11(b) for it to be compatible with our MATLAB code for periodic boundary conditions in x and y directions. There exist other choices of RVEs that may be more computationally efficient but require another set of scripts. Moreover, we want the RVE to have a complete void in the middle for better visualizing the deformation.

Also, the holes next to the edge of the finite-sized sample were cut in half to minimize the boundary effect.

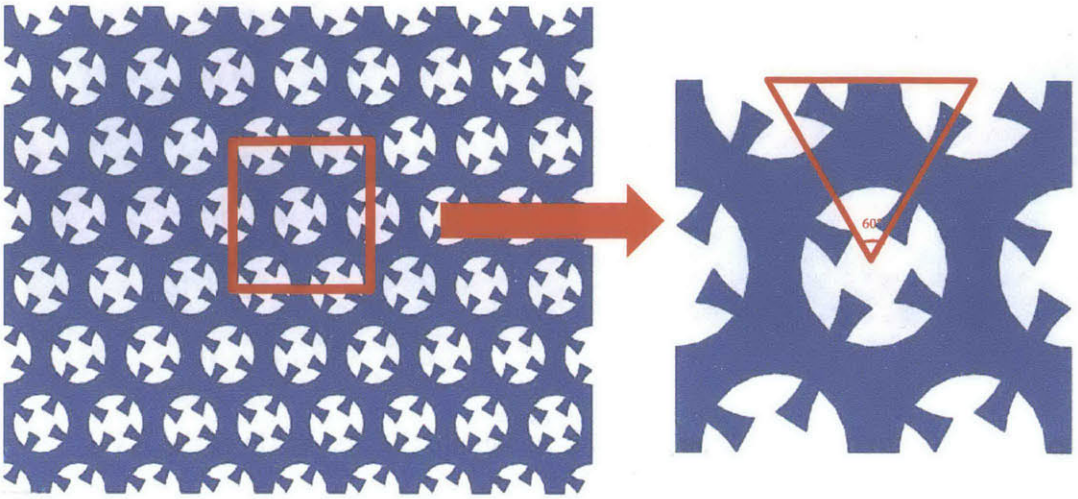

Figure 4.11 (a) a finite-sized sample with a 7 × 8 hexagonal array of circular holes with nubs; (b) a RVE representing its infinite periodic counterpart.

Figure 4.12 presents the first buckling mode of the structure. A different pattern from the matrix with holes on a square lattice is observed. The circular holes morphed into ellipse-like holes that alternate direction from row to row, clearly indicating a different mechanism from that of the square array. This distinctive pattern transformation is a result of critical intervoid shear instability, which is discussed in detail in Bertoldi, Boyce et al. 2008 [1]. An important consequence of this shear instability mechanism is that the contact nubs which had been aligned were shifted due to the shear deformation and thus no connections were able to be made upon buckling. This is also expected to happen in matrix with a staggered array of voids.

In a word, elastomeric matrix with a hexagonal or staggered array of holes is not suitable for the design of conductive pathways due the nub shifting resulting from shear instabilities.

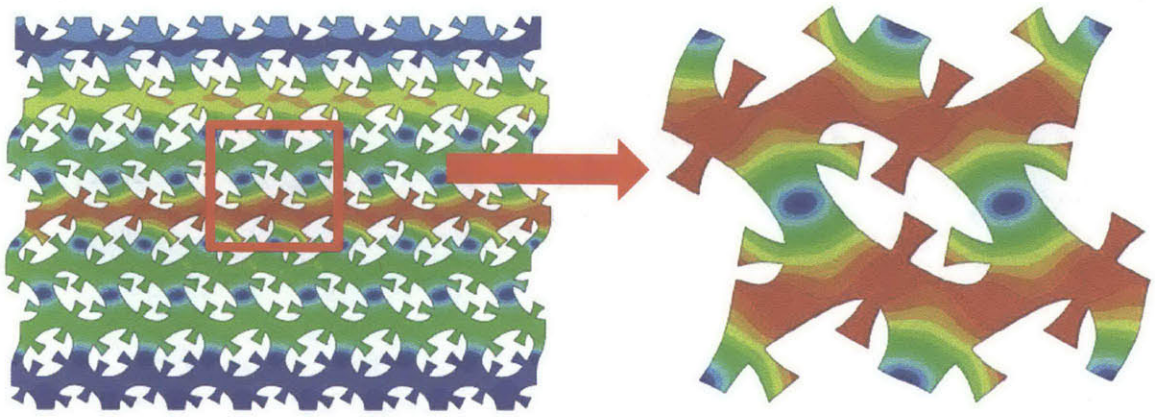

Figure 4.12 (a) first mode of the finite-sized sample (b) first mode of the RVE

4.6 References

[1] K. Bertoldi, M. C. Boyce, S. Deschanel, S. M. Prange, and T. Mullin, "Mechanics of deformation-triggered pattern transformations and superelastic behavior in periodic elastomeric structures," J. Mech. Phys. Solids, vol. 56, no. 8, pp. 2642–2668, 2008.

[2] J. Shim, S. Shan, A. Košmrlj, S. H. Kang, E. R. Chen, J. C. Weaver, and K. Bertoldi, "Harnessing instabilities for design of soft reconfigurable auxetic/chiral materials," Soft Matter, vol. 9, no. 34, p. 8198, Aug. 2013.

Chapter 5
Micromechanical model based design of conductive pathways

In Chapter 4, we introduced a novel design feature which we referred to as "contact nubs" and demonstrated how connections are made when the circular holes transform into the elliptical shape. We also investigated the effect of nub geometry on the structural behavior. Thus far, however, we have not addressed the question on how to make connections between the voids.

In this chapter, we will introduce another design feature: the conductive pathways. By adding a conductive layer on the substrate, we are able to activate a conductive pathway when opposing nubs make contact. In general, the conductive path can be thermal, mechanical or electrical, but here, we will focus on the electrical conductivity for its application in flexible circuits.

5.1 Modeling rationale for thin film bonded to an elastomer substrate

To form electrical conductive pathways, or conductive patterns, the most common way is to bond a layer of thin film to the substrate. Traditionally, the film is made of metal for its high electrical conductivity. But recently, with advances in 3D printing technology and its application in printed electronics, conductive ink, a special ink that conducts electricity by adding silver nanoparticles or graphene into a solvent, is gaining more and more attention for its operational ease and printing flexibility.

When one material is adhered to another material (i.e. the thin film and the substrate in our case) upon deformation, several possible scenarios might happen due the mismatch in material properties of the two materials and the loading condition.

1) When the load is tensile and the film and the substrate are perfectly bonded with each other, they will either stretch together like a single material until one of them (usually the thin

film because it is stiffer and also has a smaller strain to break than the substrate) ruptures at a critical stress or strain, as shown in Figure 5.1(a).

2) When the load is compressive and the film and the substrate are still perfectly bonded with each other, wrinkling would happen (i.e. the film buckles into multiple sine waves) upon reaching a critical load, as is shown in Figure 5.1(b).

3) When the film and the substrate are not so well bonded, at some point of deformation, the film detaches from the substrate. This can happen i either compression or tension and is called delamination. Figure 5.1(c) shows that the film debonds and assists the rupture when stretched, while Figure 5.1(d) shows the detachment of the film during compression.

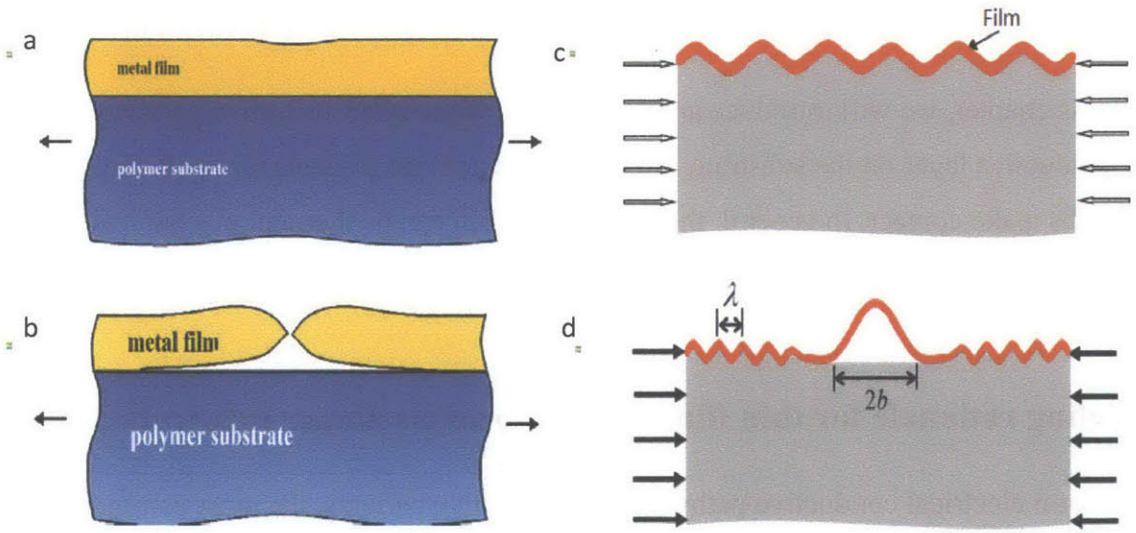

Figure 5.1 (a) A film stretches with the substrate when well bonded to the substrate. (b) A film wrinkles under compressive load when well bonded to the substrate. (Taken from Li, Suo et al. 2005[1]) (c) A film detaches from the substrate and ruptures under tensile load. (d) A film detaches from the substrate under compressive load. (Taken from Huang, et al. 2012)

Modeling a substrate with a film coating requires a full three-dimensional analysis. The film is taken to be perfectly bonded to the substrate and is modeled as linear elastic at all strain levels of our interest so that fracture will not occur. Given the above discussions, in the following sections we will focus on the effect of elastic properties and geometrical features of the film on the 2D in-plane behavior of the structure. Note that the modeling space is in 3D because of the film layer.

5.2 Three dimensional periodic structures

The finite element analyses of the periodic elastomeric substrate were previously all performed in 2D, assuming plane strain condition. This was sufficient for the study of the behavior of the elastomeric substrate alone since there is only one material. Also, it is computationally efficient to conduct 2D analysis.

However, when taking the film coating into account, the modeling space needs to be 3D, even though we are still only focused on 2D in-plane behaviors. Therefore, it is important to understand the effect of modeling a 2D plane strain condition in a 3D space. A MATLAB code for generating ABAQUS input files for 3D periodic boundary conditions was developed based on the code for 2D. The code is provided in the Appendix.

Since specimens of different void-volume fractions shows the same buckling shape, we only examine the specimen of $\psi = 50\%$ for various relative thicknesses t/R ($t = 1/8, 1/4, 1/2, 5/4$), where R is the radius of the hole. Figure 5.2 shows the detailed dimensions of the specimen we tested.

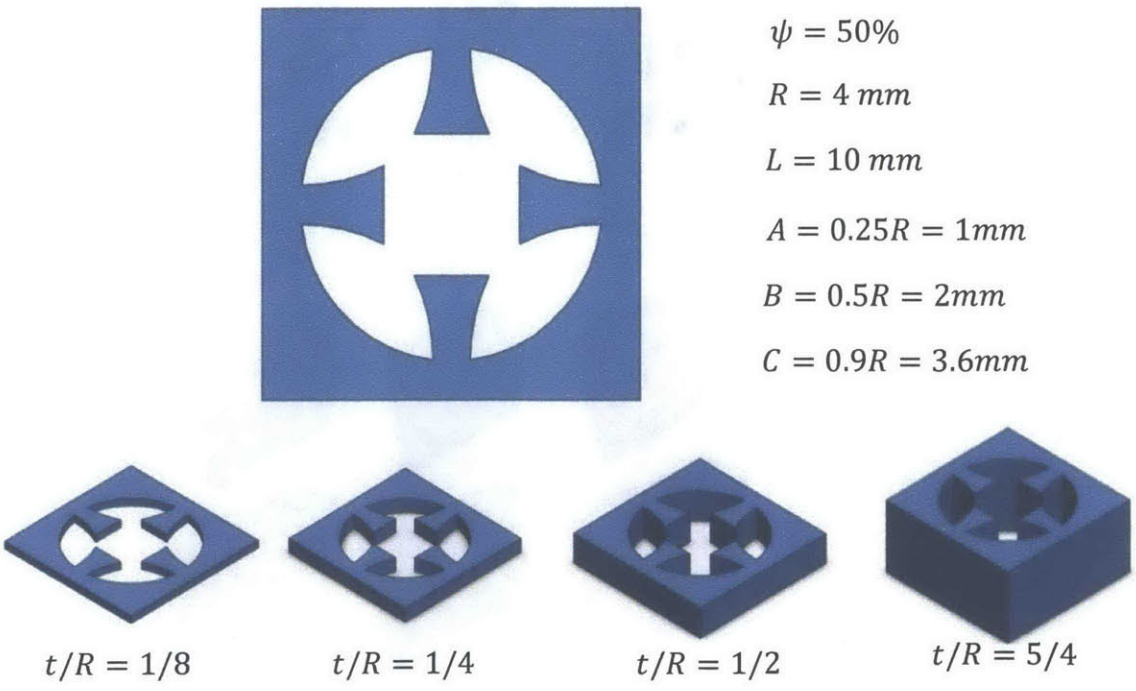

Figure 5.2 Specimen dimensions

Following the approaches in Chapter 3, Refined Eigen Analysis was performed for RVE sizes up to 8×8. The front and back surfaces of the structure were constrained in such a way that they could only deform within their planes. Hence the simulations were essentially a 2D plane strain uniaxial compression but were modeled in 3D space.

Since we are essentially doing the same plane strain analysis, the buckling shapes and eigenvalues of the 3D structure should be exactly the same as the results we obtained in 2D analysis. Figure 5.3 shows the first four eigenmodes and eigenvalues of the structure of different thicknesses. As is predicted, we get the same buckling shapes and the same eigenvalues as those of 2D analyses for all thicknesses.

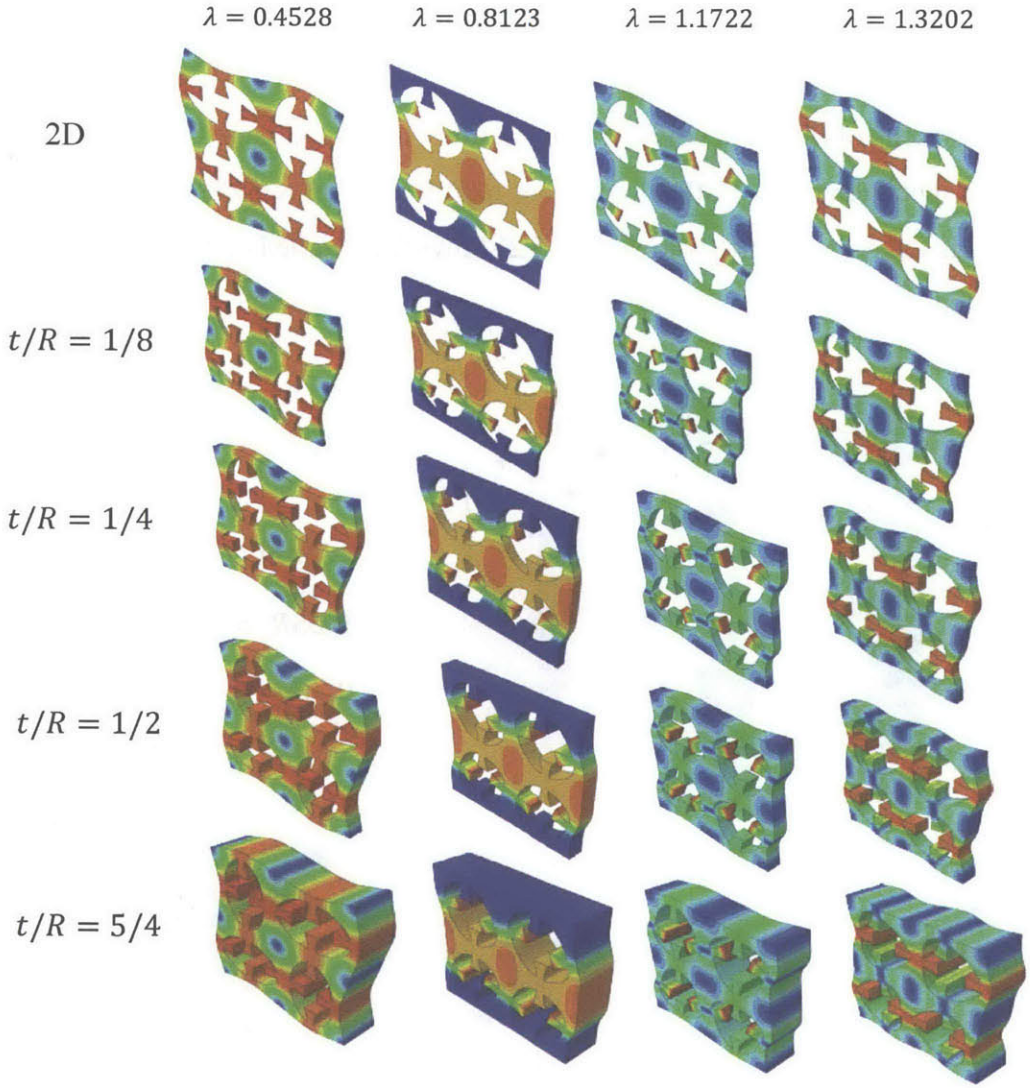

Figure 5.3 First four eigenmodes and eigenvalues of the 2D structure (plane strain) and the same structure with different thicknesses t/R ($t = 1/8, 1/4, 1/2, 5/4$)

We also plot a stress-strain curve for $t/R = 1/8$ and $t/R = 1/4$ to compare with that of the 2D specimen. Again, as shown in Figure 5.4, the three curves almost identical.

The results in Figure 5.3 and 5.4 verify the validity and robustness of our code for 3D periodic boundary conditions, and we are now in a good position to study the behavior of 3D structures with thin film coating.

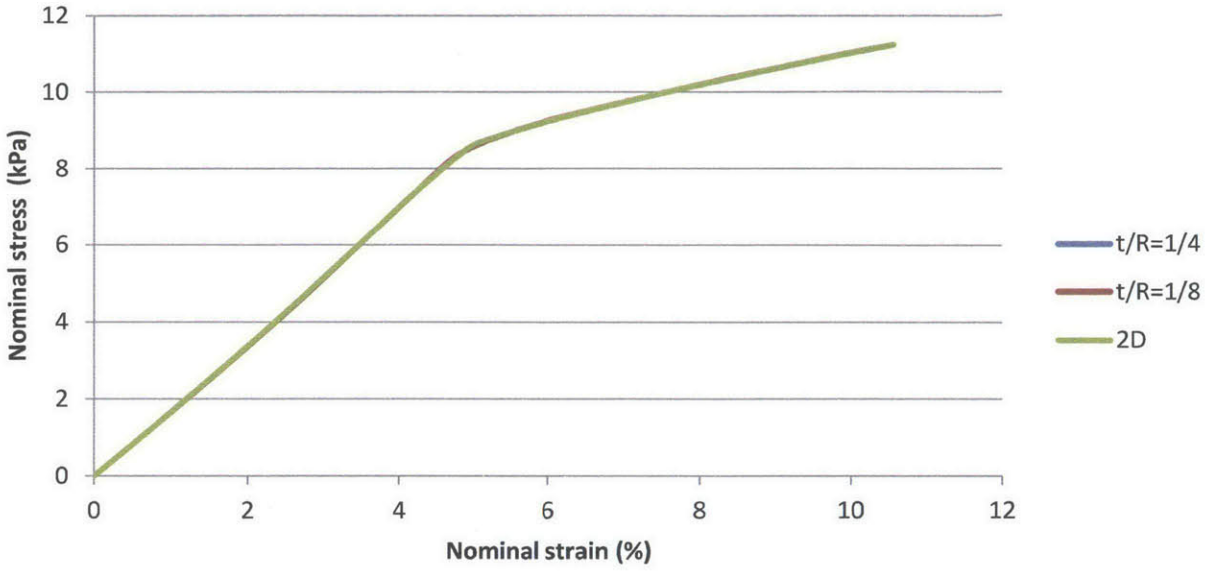

Figure 5.4 Nominal strain vs. nominal stress for 2D structure and 3D structures with thickness $t/R = 1/8$ and $t/R = 1/4$

5.3 Design of conductive pathways

Figure 5.5(a) depicts the undeformed configuration of the elastomeric substrate with circular holes in a square array, while Figure 5.5(b) depicts the buckled configuration. There are a number of ways of making connections between the voids based on the shape in Figure 5.5(b). As a result, different conductive pathways on a macroscopic scale can be formed. Figure 5.6 depicts two schematics of potential conductive pathways which we will design to be active in the buckled configuration and inactive in the undeformed state in the following sections. Figure 5.6(a) represents a conduction that goes diagonally across the substrate, while Figure 5.6(b) represents a conduction that is perpendicular to the substrate.

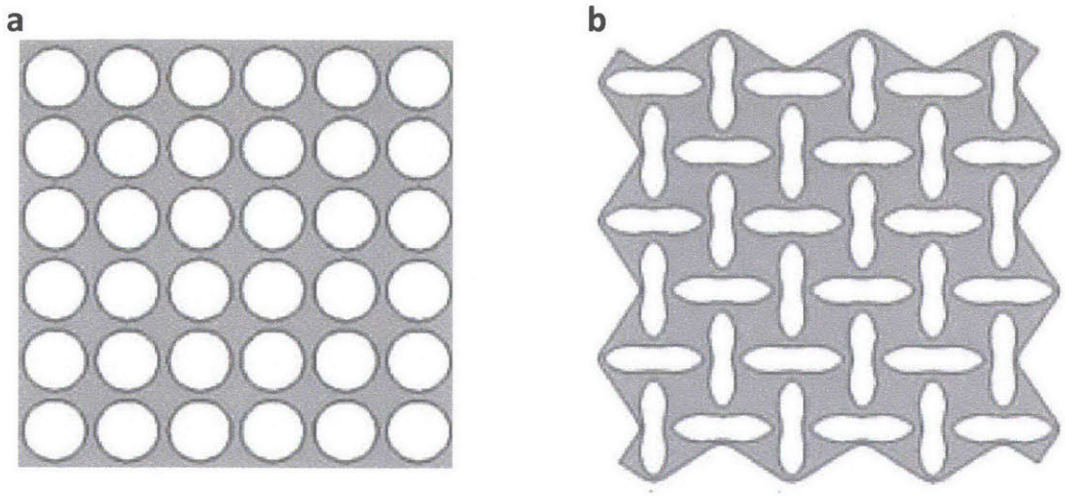

Figure 5.5 Transformative patterned elastomeric materials in undeformed and deformed states

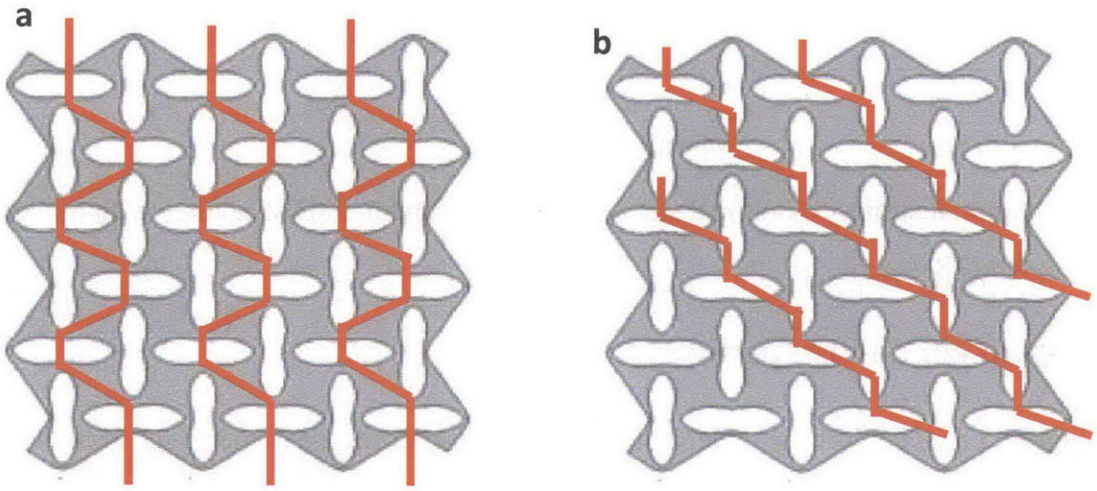

Figure 5.6 Potential conductive pathways on the deformed patterned structure

In order to achieve the conductive pathways depicted in Figure 5.6(a), we need a 2×2 RVE with nubs and thin film coating shown in Figure 5.7. Note that besides the coating on top of the substrate, the lower ends of the nubs are also fully covered with a layer of thin film to ensure full contact between the mating nubs. We will look into the effects of conductive line stiffness, conductive line width and conductive line pattern in the following sections.

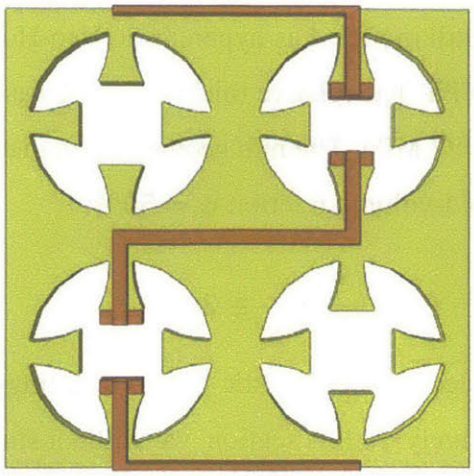

Figure 5.7 a 2 × 2 RVE with nubs and thin film coating to realize the conductive pathway depicted in Figure 5.6(a)

5.3.1 The effect of film layer thickness and film stiffness

Metal film and conductive ink are the most commonly used coating materials for conductive lines. To model a metal, a representative Young's modulus of 100 GPa is taken, while the Young's modulus of conductive ink can range from 1 MPa to 1 GPa depending on the ink component and drying time. Also, depending on the 3D printing technique, the coating film thickness can range from 1 μm to 1 mm. Since we will be using conductive ink in our experiments, we'll mainly focus our attention within this range.

In order to analyze the effect of adding a film coating on buckling modes and post-buckling behaviors of the substrate, we kept the substrate properties constant and simulated films of various elastic moduli and thicknesses. To enable our results to be applicable across all length scales, only the ratio of the elastic properties and geometrical features between the two materials were considered.

The parameters taken into account in the model are listed below:

- Relative substrate thickness: t_s/R
- Relative film thickness: t_f/R
- Substrate initial Young's modulus: E_s
- Film Young modulus: E_f

The substrate material was still modeled as hyperelastic Neo-Hookean model, with an initial shear modulus μ_0 of 0.029 MPa. The relative thickness t_s/R was 1/4. Using (5.1), the initial Young's modulus E_0 was 0.087 MPa. The nub geometry parameters used were $A = 0.25R, B = 0.5R, C = 0.9R$. The void-volume fraction $\psi = 50\%$.

$$E_0 = \frac{9\kappa\mu_0}{3\kappa + \mu_0} \cong 3\mu_0 \tag{5.1}$$

The film material was modeled as linear elastic with t_f denoting thickness and E_f denoting Young's modulus, respectively. In this section, we will not study the effect of film line width. So the film line relative width d/R was kept constant at $3/40$.

A parametric study was performed using finite element analysis with 3D periodic boundary conditions imposed. A total of nine specimens were examined. Table 5.1 shows the detailed elastic moduli and thickness used for each specimen. The results are reported in Figure 5.8, 5.9 and 5.10.

Table 5.1 Film elastic moduli and thickness

	$t_s/t_f = 10^3$	$t_s/t_f = 10^2$	$t_s/t_f = 10^1$
$E_f/E_s = 10^6$	Specimen 1	Specimen 2	Specimen 3
$E_f/E_s = 10^2$	Specimen 4	Specimen 5	Specimen 6
$E_f/E_s = 10^1$	Specimen 7	Specimen 8	Specimen 9

When the film is of very high stiffness compared to the substrate (see specimen 1, 2 and 3 in Figure 5.8), the eigenvalue and buckling modes are greatly affected by the film. This can be the case for most metal films boned to a PDMS substrate. The stiffness of a metal is usually 100 GPa, while the stiffness of a PDMS is about 1~10 MPa.

First, an increase in the eigenvalues is clearly observed, which means it requires more force to onset the buckle. For example, the eigenvalue of specimen 3 is 20% higher than that of the 2D counterpart without coating.

Another effect of having a stiff coating material is that it will alter the buckling shape (see specimen 2 and 3) because the stiff film is not easy to stretch or bend. As a result, the film

line just rotates like a rigid body, causing the mismatch of the nubs and failure to make contact when buckling occurs.

Reducing the thickness of the film helps the structure to buckle to desired shape, and yet this is not a very effective approach. As can be seen in specimen 1, even if the thickness of the film is $1/1000$ of that of substrate, the buckling shape is still slighted changed by the film.

Therefore, in order to reduce the effect of the stiffness mismatch, the film should have an ultrathin thickness less than $1/1000$ of that the substrate if the film is much stiffer than the substrate. However, for freestanding ultrathin metal films, they usually rupture at a very small strain (~1%) [2]–[4]. But they have also been experiments that show that the rupture strain of thin metal film is of large disparity, ranging from less than one percent to few tens of percent [5]–[11].

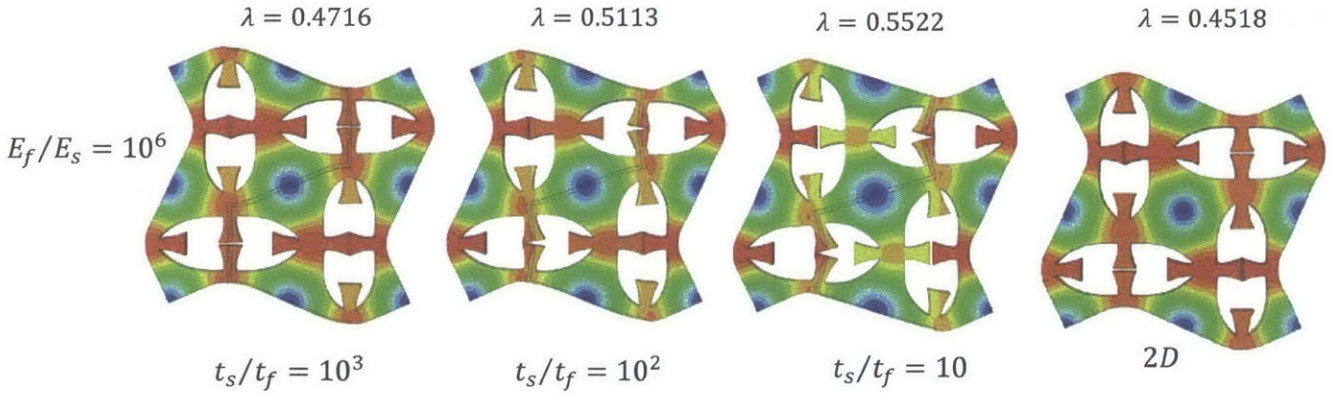

Figure 5.8 First buckling mode and eigenvalue of Specimen 1,2,3 and 2D strucutre (from left to right)

For the case where the film is of intermediate stiffness (see specimen 4, 5 and 6 in Figure 5.9), our design of conductive pathways works well when the film thickness t_f is less than 1 percent of t_s. When the layer thickness continues to increase, the difference between the stiffness of the substrate and coating begins to play a bigger role of determining the overall behavior of the structure. As is clearly shown in Figure 5.9, the nubs of specimen 6 start to rotate with the conductive line when the thickness ratio is 1: 10.

When the film stiffness is close to the substrate stiffness (see specimen 7, 8 and 9 in Figure 5.10), even though the thickness is as thick as 10 percent of the substrate, the effect of the mismatch in stiffness is still negligible (See specimen 9).

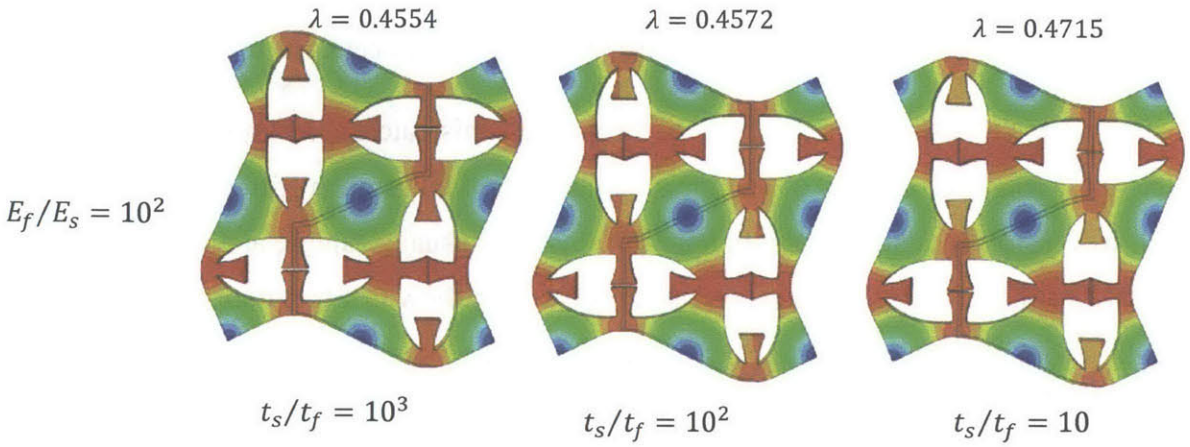

Figure 5.9 First buckling mode and eigenvalue of Specimen 4, 5 and 6 (from left to right)

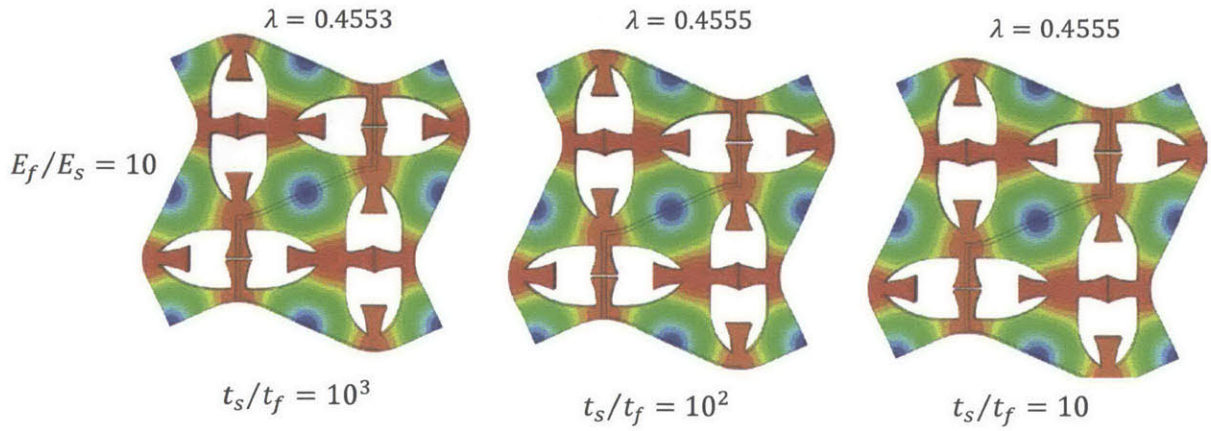

Figure 5.10 First buckling mode and eigenvalue of Specimen 7, 8 and 9 (from left to right)

To explore further on the effect of film thickness and stiffness on the coated substrate behavior, stress and strain curves were plotted for specimen 3 ($E_f/E_s = 10^6$,$t_s/t_f = 10$) and specimen 7($E_f/E_s = 10$,$t_s/t_f = 10^3$) in Figure 5.11. Specimen 3 is the structure with the thickest coating and the stiffest film material, while specimen 7 has the thinnest coating and the most compliant film material.

As is predicted, the structure with the thickest coating and the stiffest film material (i.e. specimen 3) is characterized by a much high buckling stress and a "stress plateau" with a much larger slope than that of specimen 7 after the buckling.

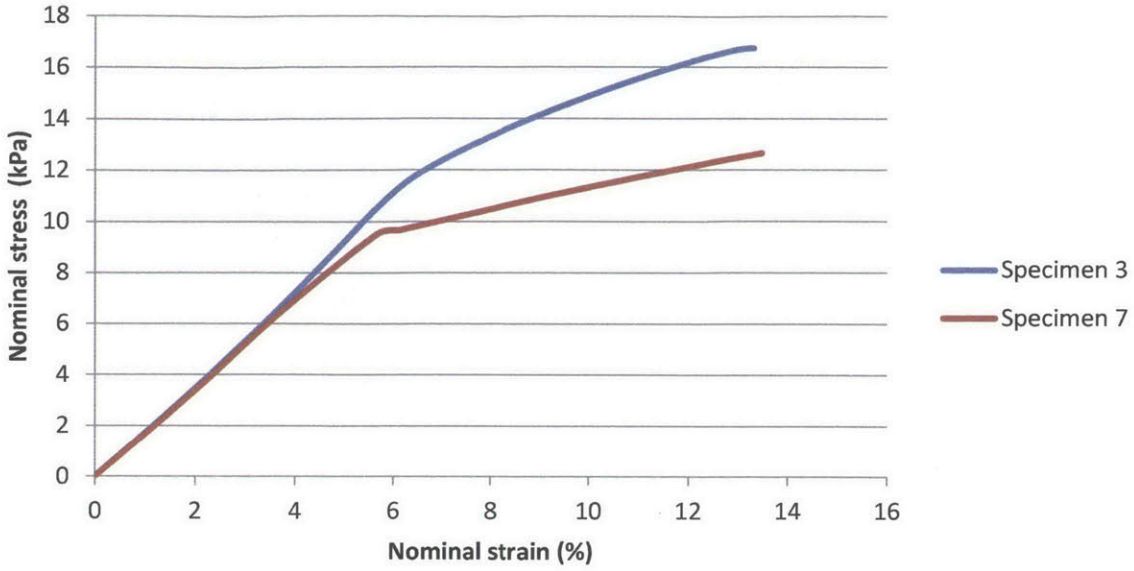

Figure 5.11 Nominal strain vs. nominal stress for specimen 3 and 7

It is also important to study the strain distribution within the RVE, especially the strain level in the film. Figure 5.12 shows the principal strain and strain in the 11 direction (perpendicular to the compression direction). It can be seen the film is mostly stretched in the middle region as it deforms with the substrate.

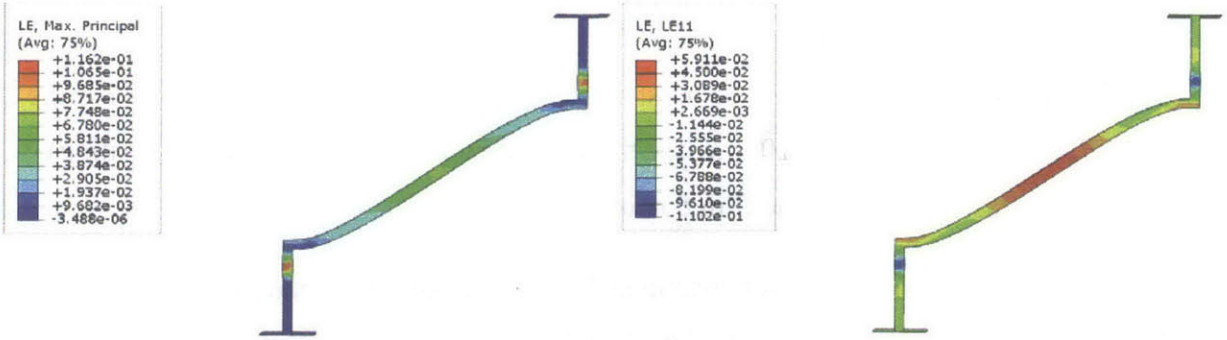

Figure 5.12 Strain levels within the film

5.3.2 The effect of conductive line width

It is expected that the narrower the conductive line, the less the effect on structure behavior. However, narrow lines also mean less reliable conduction. So it is a design tradeoff between the film width and the reliability of conduction. Here, we are going to briefly explore the effect of conductive line width. Figure 5.13 shows RVEs of various conductive line widths.

In light of the results in the prior section, we vary the conductive line width on specimen 3 and specimen 7. The reason for choosing these two are that specimen 3's buckling mode was greatly affected by the existence of the film and specimen 7's buckling mode was slightly changed by the coating. We hope to find out whether reducing the conductive line width would minimize the effect. The conductive line width was also normalized by R. The results are presented in Figure 5.14 and Figure 5.15.

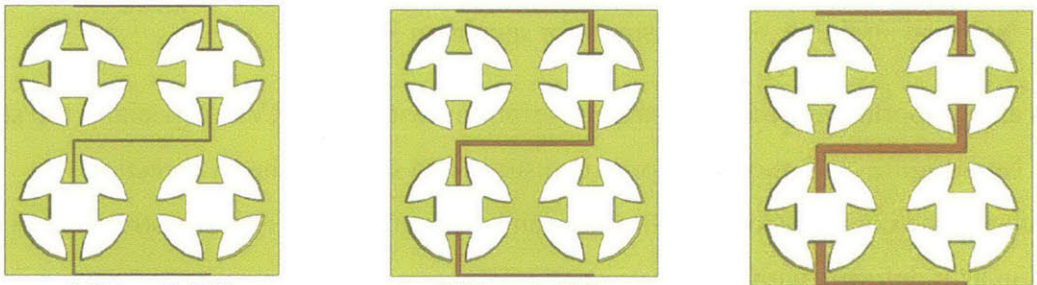

Figure 5.13 RVEs with conductive line width $d/R = 1/40, d/R = 3/40$ and $d/R = 3/20$

Recall that specimen 3 is the one with $E_f/E_s = 10^6$ and $t_s/t_f = 10$ (i.e. the thickest and the stiffest film coating) and is found to be most affected by the film coating. Specimen 7 is the one with $E_f/E_s = 10^3$ and $t_s/t_f = 10^3$(i.e. the thinnest and the most compliant film coating) and is found to be least affected by the film coating.

Figure 5.14 shows the results for specimen 3. It can be seen that decreasing the coating line width does not help reduce the effect of stiffness mismatch. Even the coating line is as thin as $d/R = 1/40$, which is close to the limit of the conductive line width required to make conductions, the nubs are still interfered by the rigid rotation of the film line.

Figure 5.15 shows the results for specimen 7. Being the structure with the thinnest and most compliant film coating, it is expected for the coating line to have negligible effect on the buckling modes, regardless of the width. Surprisingly, just doubling the film line width from $d/R = 3/40$ to $d/R = 3/20$ would cause a change in the buckling shape.

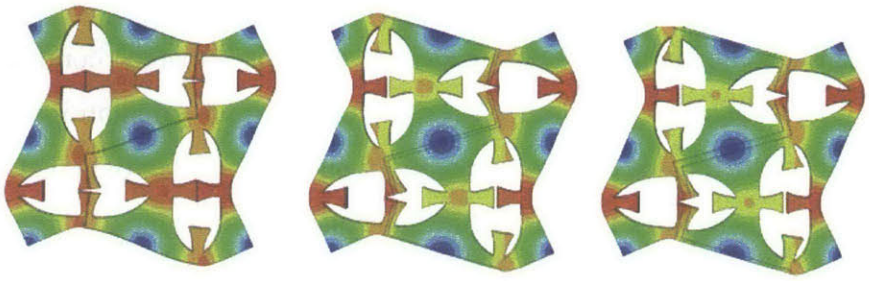

Figure 5.14 Specimen 3 with conductive line width $d/R = 1/40, d/R = 3/40$ and $d/R = 3/20$

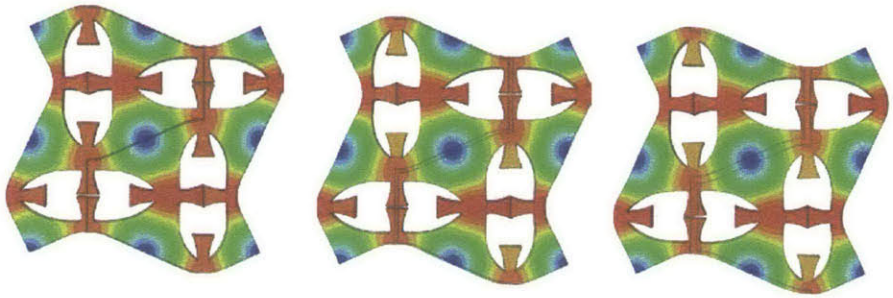

Figure 5.15 Specimen 7 with conductive line width $d/R = 1/40, d/R = 3/40$ and $d/R = 3/20$

5.4 Discussion on the design of conductive pathways

The goal of this chapter is to explore the effect of coating film thickness, width and stiffness on the electrical and mechanical behavior of the coated elastomeric substrate.

In order to achieve better electrical performance, the conductive line needs to be wide enough and thick enough, because the electrical resistance of the conductive material is inversely proportional to the cross-sectional area of the conductive line. In other words, larger cross-sectional area leads to higher conductivity.

On the other hand, in order to take most advantage of the buckling shape of the elastomeric substrate, the conductive line needs to be as narrow and thin as possible, because the buckling shape of a compliant substrate is very sensitive to the addition of another stiff material.

Therefore, it is a tradeoff between electrical performance and the mechanical behavior. It is impossible to maximizing one without compromising the other.

The results we obtained from this chapter can provide us guidance for tailoring the elastic properties and geometric features of the film to satisfy specific design requirements.

One important conclusion from the finite element analysis is that the compliance of the film plays a much bigger role than the geometry (i.e thickness, width, orientation) of the film. In particular, when the film stiffness is of the same order or one order higher than that of the substrate, even if the film is as thick as $1/10$ of the substrate, it is still able to stretch or bend with the substrate maintaining the same buckling shape of the structure as it has without the coating. However, geometrical features become equally important when the film is much stiffer than the substrate. For instance, when the film is 10^6 stiffer than the substrate, the thickness needs to be less than $1/1000$ that of the substrate so as not to influence the buckling shape.

In terms of electrical performance, metal film has a much higher conductivity than any existing type of conductive ink. For example, copper has a volume resistivity of $1.68 \times 10^{-6}\ \Omega \cdot$ cm and silver has a volume resistivity of $1.59 \times 10^{-6}\ \Omega \cdot$ cm, while the volume resistivity of conductive ink ranges from $1 \times 10^{-4}\ \Omega \cdot$ cm for silver particle-based conductive ink to 100 $\Omega \cdot$ cm for carbon particle-based conductive ink. Just by simple comparison, the volume resistivity of metal is nearly two orders of magnitude less than that of the best conductive ink available.

If we are to use metal for better conductivity, we need to have a very thin layer of film to minimize the influence of the high stiffness of the metal on the buckling shape of the circuit. Consider the design of a 1mm thick flexible circuit with copper coating. The Young's modulus of the circuit substrate is 1MPa. We know that copper has a Young's modulus around 100 GPa, so the thickness of the copper should be less than 0.001 mm, which is 1 μm. Advances in micro and nano fabrications nowadays have made it possible to manufacture copper layers of thickness in the order of nanometers, though it does require a fine and complicated manufacturing process.

Metal films, due to their excellent conductivity, appear to the best choice for fabricating flexible circuits and yet conductive ink has one big advantage over metal films, that is, the ease in operation and the flexibility in printing patterns. One can simply load the conductive ink in

any ink-jet printer and print any complex conductive patterns on the substrate just as we normally print on paper.

In summary, if we need to design a device that requires high conductivity and high precision, we should use ultrathin metal films. If we are to manufacture a large number of devices that do not require high conductivity, conductive ink offers a fast, easy and cost effective alternative.

For the purpose of this study, we use conductive ink for our experiments for its operational ease. The conductivity of the ink is found to be sufficient to demonstrate the key ideas of this study. More details about conductive ink and the fabrication process are provided in the following chapter.

5.5 References

[1] T. Li, Z. Suo, S. P. Lacour, and S. Wagner, "Compliant thin film patterns of stiff materials as platforms for stretchable electronics," J. Mater. Res., vol. 20, no. 12, pp. 3274–3277, Mar. 2011.

[2] D. Baral, J. B. Ketterson, and J. E. Hilliard, "Mechanical-Properties of Composition Modulated Cu-Ni Foils," J. Appl. Phys., vol. 57, no. 4, pp. 1076–1083, 1985.

[3] H.-J. Lee, P. Zhang, and J. C. Bravman, "Tensile failure by grain thinning in micromachined aluminum thin films," J. Appl. Phys., vol. 93, no. 3, p. 1443, Feb. 2003.

[4] D. W. Pashley, "A Study of the Deformation and Fracture of Single-Crystal Gold Films of High Strength Inside an Electron Microscope," Proc. R. Soc. A Math. Phys. Eng. Sci., vol. 255, no. 1281, pp. 218–231, Apr. 1960.

[5] T. Li, Z. Huang, Z. Suo, S. P. Lacour, and S. Wagner, "Stretchability of thin metal films on elastomer substrates," Appl. Phys. Lett., vol. 85, no. 16, p. 3435, Oct. 2004.

[6] T. Li and Z. Suo, "Deformability of thin metal films on elastomer substrates," Int. J. Solids Struct., vol. 43, no. 7–8, pp. 2351–2363, 2006.

[7] T. Li and Z. Suo, "Ductility of thin metal films on polymer substrates modulated by interfacial adhesion," Int. J. Solids Struct., vol. 44, no. 6, pp. 1696–1705, Mar. 2007.

[8] D. Vella, J. Bico, A. Boudaoud, B. Roman, and P. M. Reis, "The macroscopic delamination of thin films from elastic substrates.," Proc. Natl. Acad. Sci. U. S. A., vol. 106, no. 27, pp. 10901–6, Jul. 2009.

[9] Y. Xiang, T. Li, Z. Suo, and J. J. Vlassak, "High ductility of a metal film adherent on a polymer substrate," Appl. Phys. Lett., vol. 87, no. 16, p. 161910, Oct. 2005.

[10] B. E. Alaca, M. T. A. Saif, and H. Sehitoglu, "On the interface debond at the edge of a thin film on a thick substrate," Acta Mater., vol. 50, no. 5, pp. 1197–1209, 2002.

[11] S. L. Chiu, J. Leu, and P. S. Ho, "Fracture of metal-polymer line structures. I. Semiflexible polyimide," J. Appl. Phys., vol. 76, no. 9, p. 5136, 1994.

Chapter 6
Experiments

Having investigated the effect of various design parameters, in order to verify the validity of our simulations we fabricated a specimen using 3D printing and casting. Uniaxial compression tests were conducted. Later in this chapter, a printed working demonstration circuit that can be turned on and off via external stimuli in the form of uniaxial compression is shown as a successful example.

In the previous chapters, we've kept all design parameters dimensionless, so that only the relative properties of materials and geometrical features matter. Therefore, the simulation results are theoretically applicable to all length scales, including the desktop-scaled physical model (~ 10 cm) we used in the experiment.

The substrate and the conductive lines were fabricated separately using distinct techniques, both of which are introduced in this chapter.

The molding and casting were performed in the Boyce lab with great help from Professor Pedro Reis in the Department of Civil Engineering at MIT. The printing of conductive pathways were performed in collaboration with Dr. Bok Yeop Ahn and Professor Jennifer Lewis at the Harvard School of Engineering.

6.1 Substrate fabrication

A silicone rubber (Vinyl Polysiloxane: Elite Double 8, Zhermack) was used to cast the experimental specimens. The material properties were tested in Chapter 2. The material behavior was found to be well captured by the Neo-Hookean model up to a strain of 35%. The shear modulus was measured to be 0.058 MPa.

The mold for casting the specimen was made using 3D printing and laser cutting. The mold comprised a base, 4 lateral walls and hundreds of pillars to shape the microfeatures of the nubs. The base and the lateral walls were made from acrylic plates (McMaster-Carr Supply Co.). A laser cutter (Epilog mini 18, Epilog Laser Corp.) was used to cut the voids with nubs. The pillars were 3D printed using the Form1 3D printer (Formlabs) having a printing resolution of 300 μm. Then the pillars were manually inserted into the base and were properly oriented because of the nubs. The holes on the base were deliberately made slightly larger than the pillars for easy insertion, but were still tight enough to prevent the uncured silicone rubber from leaking through the gap (see Figure 6.1). The silicone rubber was vacuumed for 5 minutes to remove the

air trapped during the mixing process before it was cast in the mold. The mold was then left open to air and the casting mixture cured at room temperature in just 20 minutes. After curing was completed, the walls were dismantled and pillars were removed. The final specimen and zoomed-in images of the circular holes with nubs are shown in Figure 6.2.

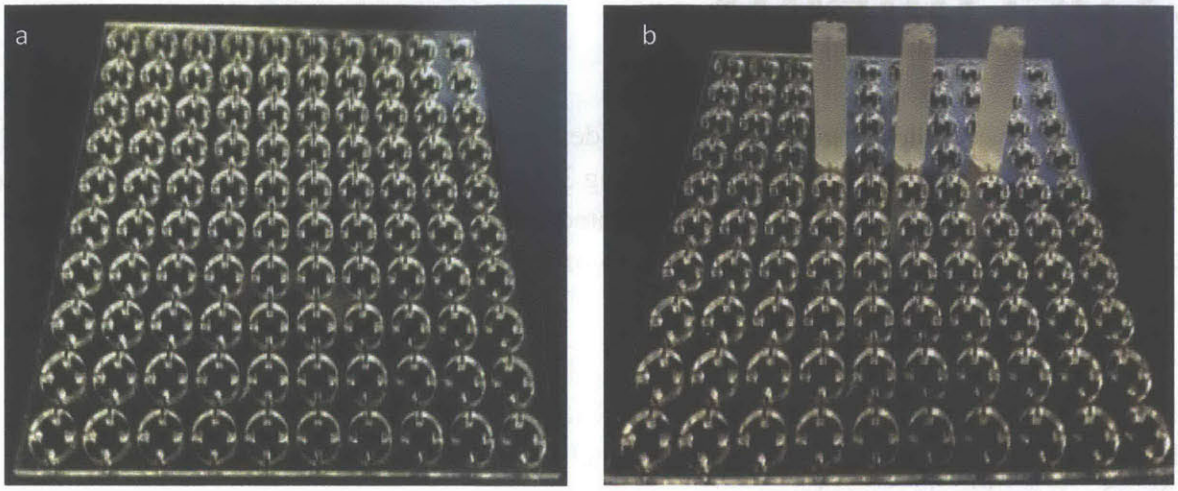

Figure 6.1 (a) Acrylic base with microstructures made by laser cutter. (b) Pillars made using 3D printer were inserted into the base.

The final specimen comprised a 10×10 square array of circular holes of 8 mm diameter with 10 mm center-to-center spacing, vertically and horizontally. There is 6 mm from the center of the lateral holes to the edge of the specimen. The microscopic geometrical parameters of the nubs are $A = 1, B = 2$ and $C = 3.6$. The overall size of the specimen is W(width)× H(height)× T(thickness)= 102 mm × 102 mm × 23 mm.

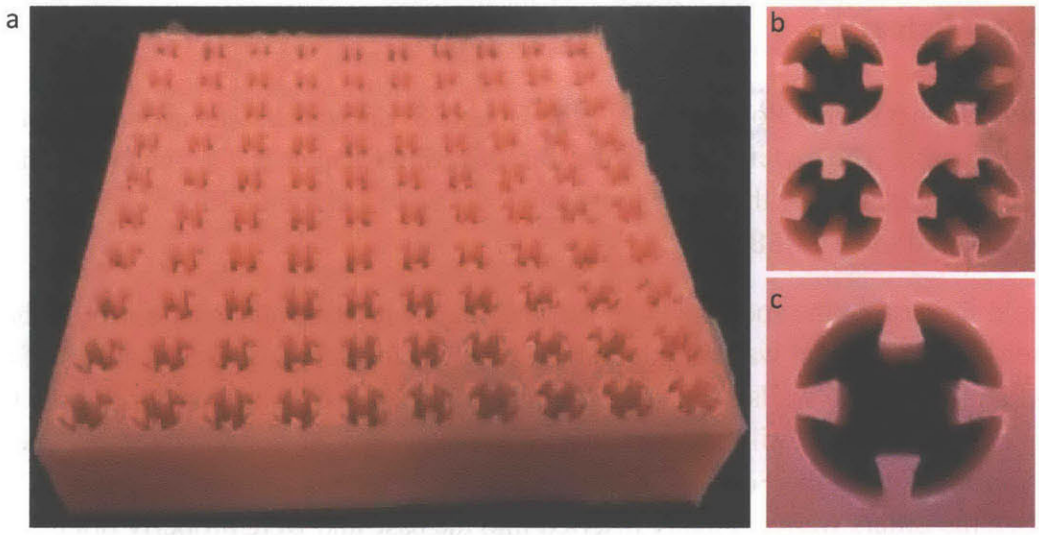

Figure 6.2 (a) Final substrate (b) Zoomed-in image of the RVE with four unit cells (top view) (c) Zoomed-in image of one circular void with four contact nubs (top view)

6.2 Conductive pathways printing

6.2.1 Conductive Ink

Conductive ink, as the term suggests, is a special ink that has electrical conductivity after printing. It is usually made by the suspension of conductive materials, such as metallic nanoparticles (silver, gold, and copper), carbon nanoparticles and carbon nanotubes (CNTs) into solvents such as toluene, α-terpineol, glycerol and water. The ink is usually not conductive before printing, but its electrical resistance reduces after solvent removal or heat treatment. The ink conductivity and mechanical property is determined by the dispersed material and the solvent. For example, silver or copper-based ink has excellent conductivity, but it is not stretchable or bendable. Carbon-based ink possesses good flexibility, but it is restricted by their relatively low conductivity [1]. A rudimentary version of ink can also be made by simply mixing conductive particles with grease without using solvent.

For the purpose of this work, the conductive pattern was printed using a commercial carbon-based conductive ink (Carbon Conductive Grease 846, M.G. Chemicals) for its low cost and stretchability. The conductive material is the mixture of carbon particles and grease. No solvent was used. The ink can be stretched up to 10% strain while maintaining a volume resistivity at about 117 $\Omega \cdot$cm.

6.2.2 Direct ink writing technique

There are different methods for printing conductive patterns such as ink jet, screen printing, flexography and lithography. Each method has its own advantages and limits. In this work, in order to achieve high efficiency, low cost and the ability to print arbitrary conductive patterns, direct ink writing is used.

Direct writing describes fabrication methods that employ a computer controlled translation stage, which moves a pattern generating device [2], [3], in our case, the ink-deposition nozzle, to create materials with controlled architecture and composition.

Figure 6.3 (a) and (b) show photos of the direct ink writing printer we used in printing the conductive pathways. As illustrated in Figure 6.3 (a), the printer comprises a three axis motion stage, an ink reservoir with nozzle, a sample stage, an air supply and an optical microscope for visualization.

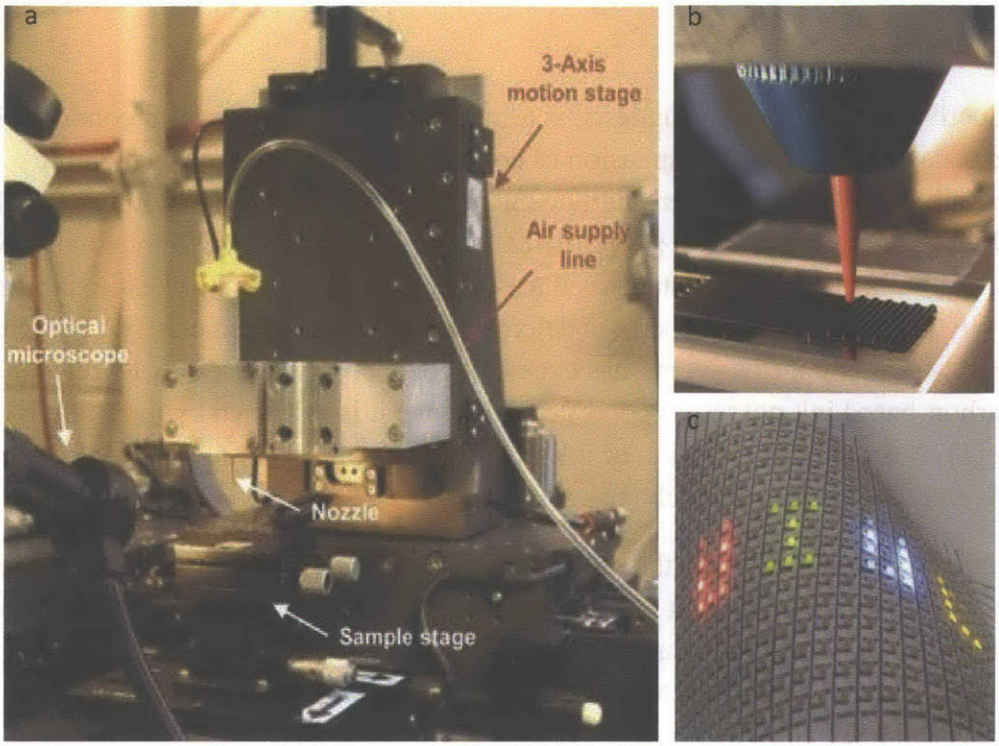

Figure 6.3 (a) 3D printer (b) printed conductive lines and nozzle (c) a printed circuit (Taken from Russo, Ahn et al. 2011 [4])

The system works as follows: First, the conductive ink is loaded into a syringe. After attaching a deposition nozzle, the ink loaded syringe is mounted onto the 3-axis printing stage, which can move up and down, back and forth, and left and right. The nozzle then is connected to an air-powered fluid dispensing system that controls the pressure applied to the syringe, so that the velocity of the ink when ejecting out of the nozzle can be controlled as well. The substrate is fixed on the sample stage and the moving speed of the nozzle is controlled by the computer. The printed features depend on ink properties (viscosity, density, etc.), nozzle diameter and printing speed. We can tailor any of the above parameters for specific printing of interest. Figure 6.3 (c) shows a circuit printed using this method.

6.2.3 Printing of conductive pathways

A carbon-based conductive ink (Carbon Conductive Grease 846, M.G. Chemicals) was used to print the conductive pattern. It has a volume resistivity of 117 Ω·cm. The conductive line was about 1mm thick and 0.6 mm wide.

Figure 6.4 shows the schematics of the desired conductive pathways (the thick lines) and the circuit components including a battery and a small LED (the thin lines). Figure 6.4(a) shows

the circuit in an inactive state with disconnected conductive pathways before deformation, while Figure 6.4(b) depicts a complete circuit that should light up the LED upon pattern transformation.

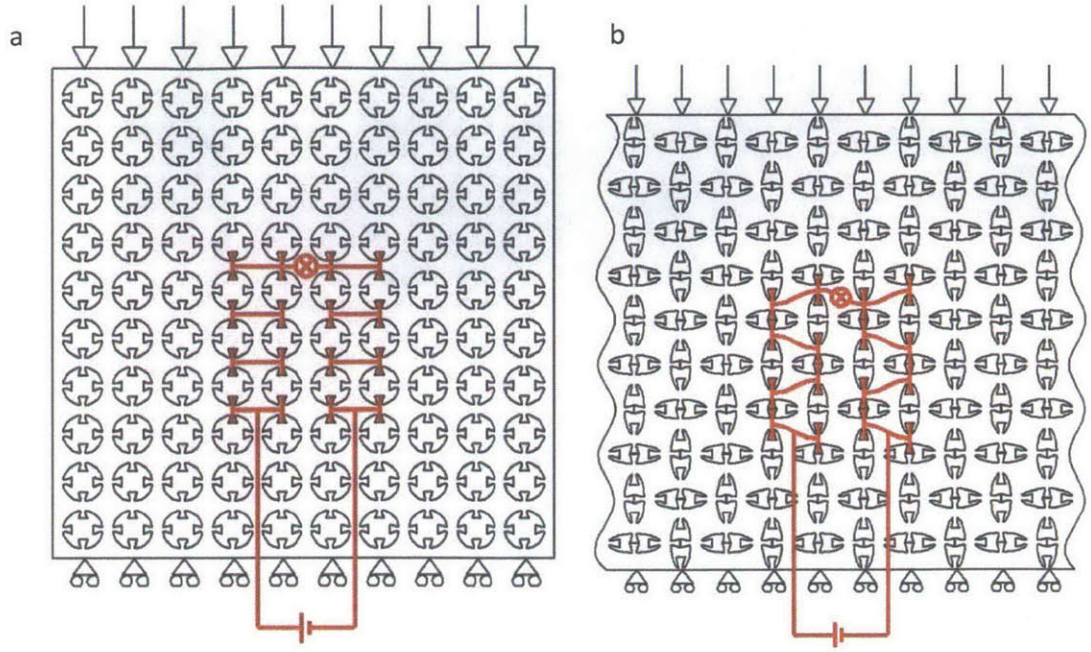

Figure 6.4 Schematics of designed conductive pathways (a) disconnected circuit in an undeformed configuration (b) connected circuit in a deformed configuration

Figure 6.5 shows the printing setup. The substrate fabricated using methods outlined in Section 6.1 was fixed on the sample platform. G-code controlling the movement of the nozzle was implemented in the computer program. The printing was performed in air at room temperature (~20 °C). Figure 6.6 shows the printed feature.

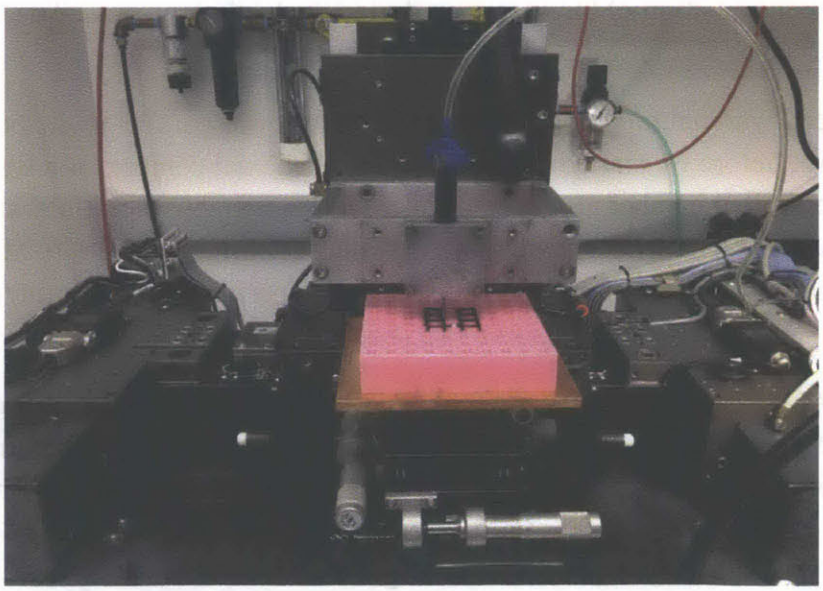

Figure 6.5 Printing setup

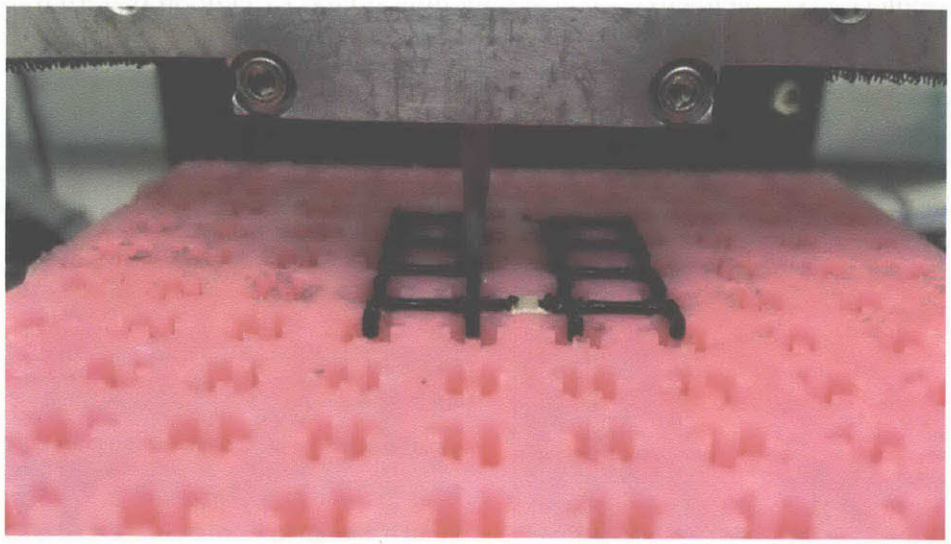

Figure 6.6 Printed conductive pathways

6.3 Experiments and results

6.3.1 Mechanical behavior of the substrate

6.3.1.1 Experiment protocol

Uniaxial compression tests were performed using a Zwick screw-driven testing machine with a 250 kN load cell. The thickness of the sample is large enough to avoid out-of-plane buckling. Moreover, the friction between the sample surface and the load cell surface is also large enough to fix the position of the specimen during the loading process. To avoid introducing unnecessary frictions, no fixture was used.

The load cell was carefully adjusted to ensure that it was parallel to the bottom supporting platform before we started the loading. Then uniaxial compression was performed in a displacement-controlled manner at different speeds of loading, but the results showed the structural response has no dependence on the rate, which confirms the validity of the quasi-static analysis in the simulations. Therefore, only the test results performed at 20 mm/min are reported.

A Nikon AF Micro Nikkor 60mm f/2.8D was used to take snapshots during the test at every time increment $\Delta t = 500$ ms. Force and displacement were recorded automatically at a time increment subject to the program. A post-processing MATLAB code was implemented to correlate the images taken by the camera with the displacement data recorded by the computer, so that we were able to identify the structure configuration at different strain levels. Also, a

nominal strain vs. nominal stress relation was computed from the force and displacement data and the specimen dimensions.

6.3.1.2 Results

Figure 6.7 shows both experiments and simulations of the pattern and its transformation. Various stages of deformation show the ability to transform the pattern and provide conductive pathways when the nubs make contact with one another. There is excellent agreement between the simulation results and the experimental images of the pattern evolutions as shown in Figure 6.7.

Excellent quantitative agreement is obtained between the stress-strain results of the finite element simulation and those from the experiment as shown in Figure 6.8. The stress-strain curve captures the linear regime, pattern transformation at critical strain and stress plateau from the accentuation of the elliptical pattern.

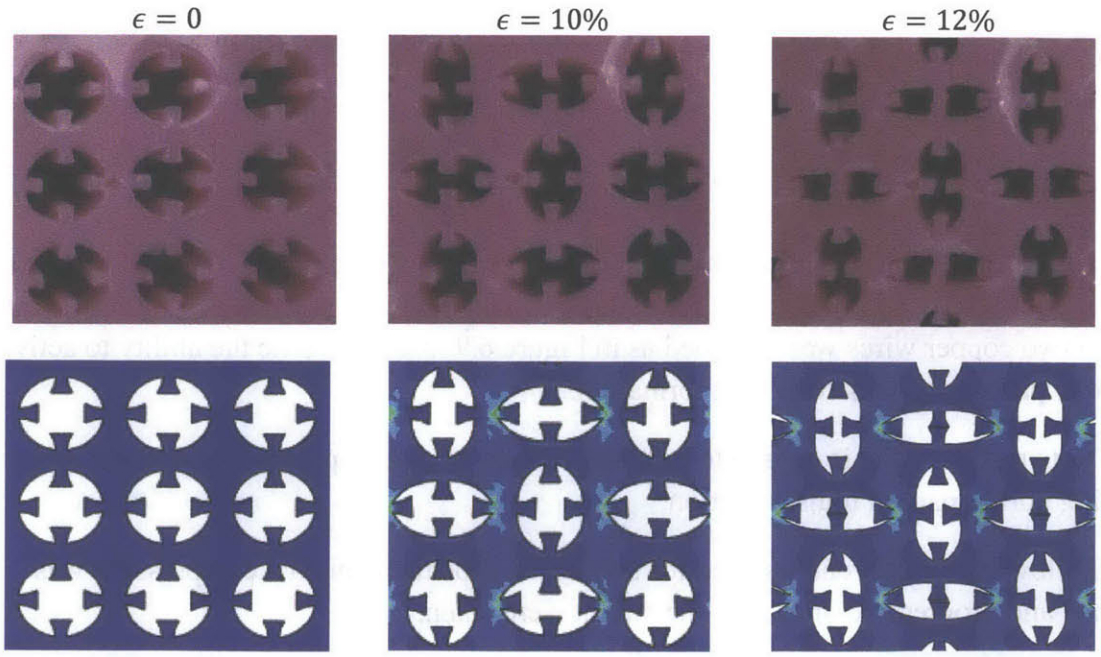

Figure 6.7 Experimental and numerical images of the specimen at different strains

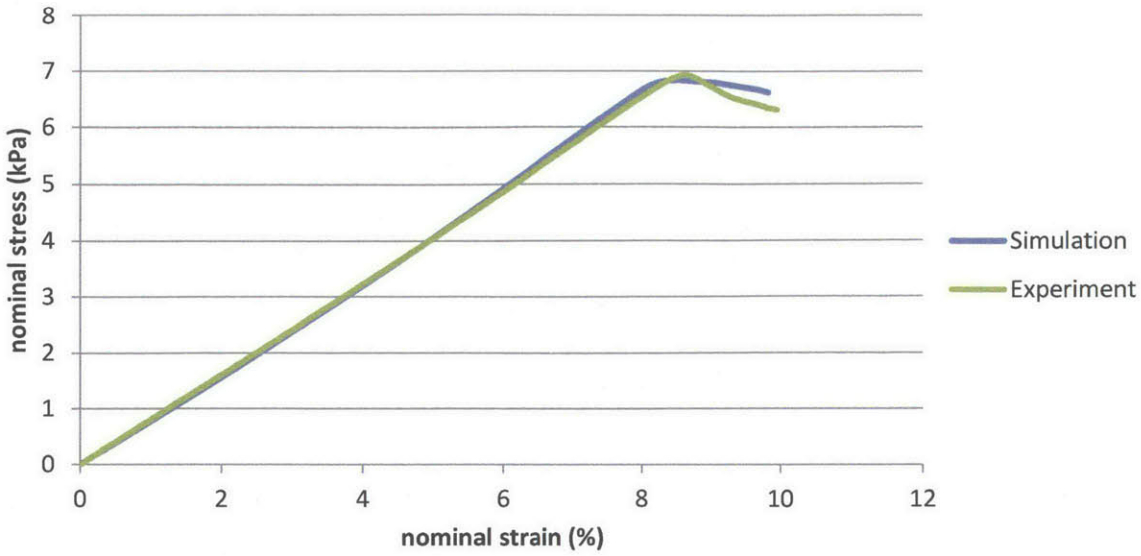

Figure 6.8 Nominal stress vs. nominal strain curve showing experimental and numerical results

6.3.2 Demonstration circuit

6.3.2.1 Experiment protocol

After the uniaxial compression test, conductive lines were printed on the substrate using the techniques discussed in Section 6.2. A simple circuit including a 9V battery, a tiny green LED and two copper wires was designed as in Figure 6.9 to demonstrate the ability to activate conductive pathways via pattern transformation.

Note that the LED is chosen to be small enough so that its presence is deemed as non-interfering during pattern transformation.

Following the approaches used for testing the substrate, uniaxial compression was performed and progressive images of the circuit were taken.

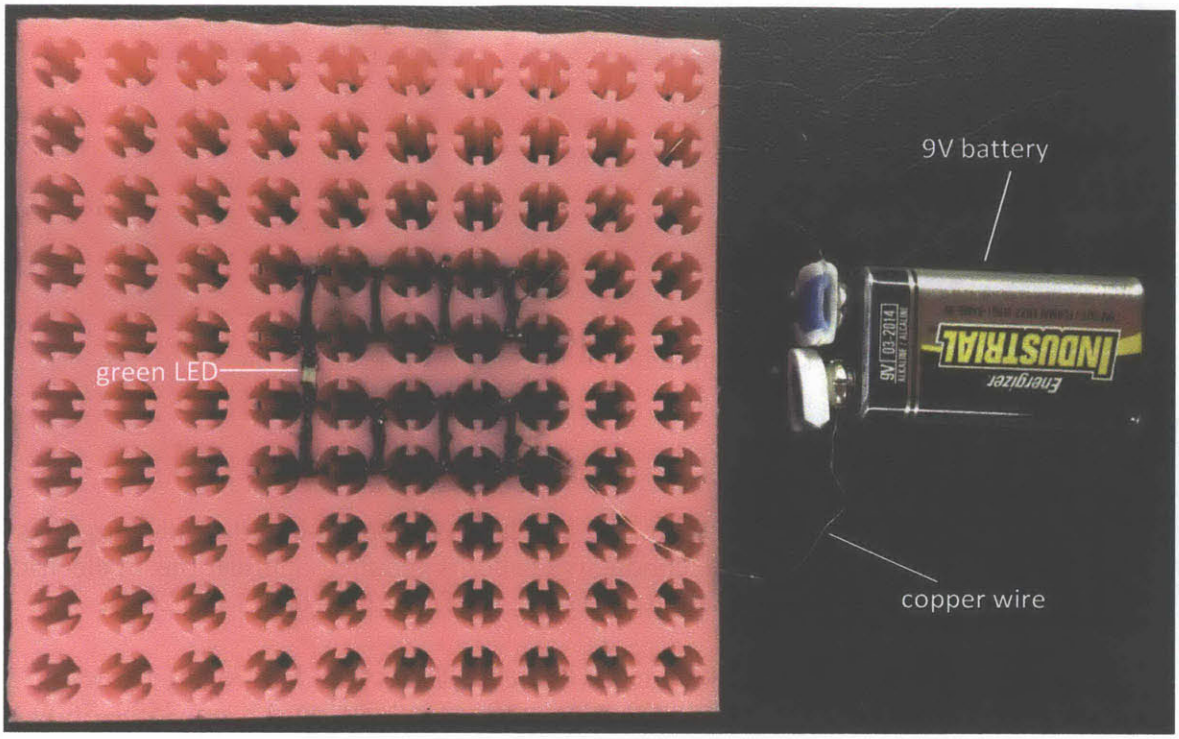

Figure 6.9 Demonstration circuit layout

6.3.2.2 Working demonstration circuit

Figure 6.10 (a), (b) and (c) show the progressive images of the circuit during uniaxial compression. Upon deformation, the nubs come closer and eventually make contact to complete the circuit and the LED lights up to demonstrate the ability to switch conductive pathways on and off. Figure 6.10 shows zoomed in images focused on the center part of the sample.

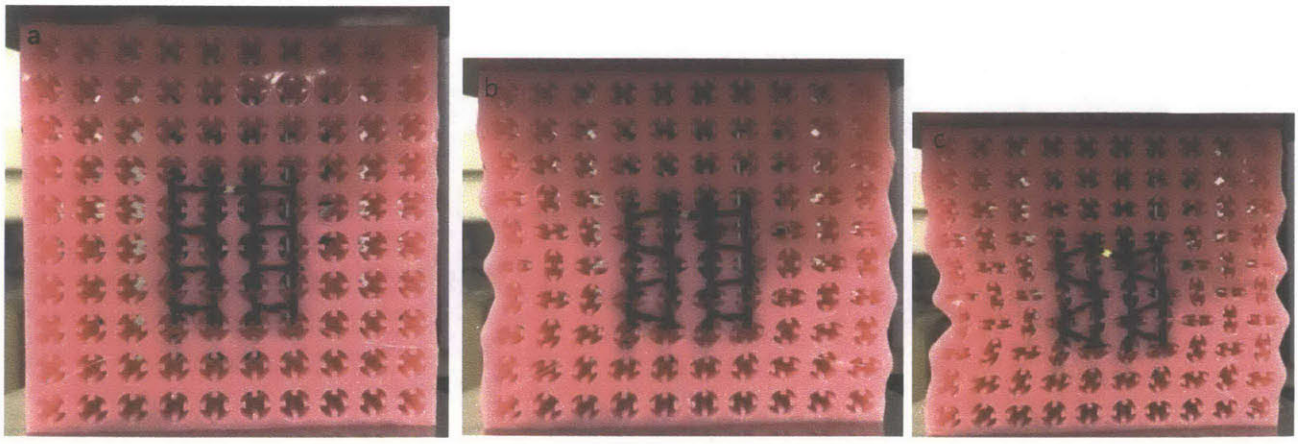

Figure 6.10 Images of progressive deformation of the demonstration circuit. (a) undeformed circuit; conductive pathways disconnected (b) deforming circuit (c) deformed circuit; conductive pathways connected to light up the LED

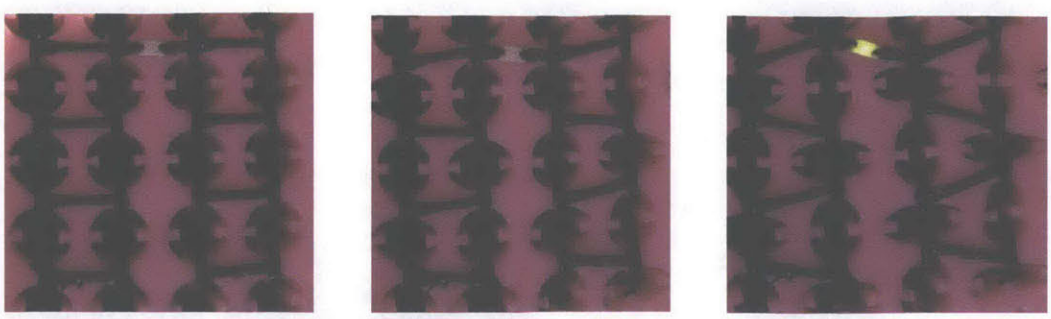

Figure 6.11 Zoomed in images of the completion of the demonstration circuit.

6.4 References

[1] L. Huang, Y. Huang, J. Liang, X. Wan, and Y. Chen, "Graphene-based conducting inks for direct inkjet printing of flexible conductive patterns and their applications in electric circuits and chemical sensors," Nano Res., vol. 4, no. 7, pp. 675–684, Mar. 2011.

[2] J. A. Lewis, J. E. Smay, J. Stuecker, and J. Cesarano, "Direct Ink Writing of Three-Dimensional Ceramic Structures," J. Am. Ceram. Soc., vol. 89, no. 12, pp. 3599–3609, Dec. 2006.

[3] J. A. Lewis, "Direct Ink Writing of 3D Functional Materials," Adv. Funct. Mater., vol. 16, no. 17, pp. 2193–2204, Nov. 2006.

[4] A. Russo, B. Y. Ahn, J. J. Adams, E. B. Duoss, J. T. Bernhard, and J. A. Lewis, "Pen-on-paper flexible electronics.," Adv. Mater., vol. 23, no. 30, pp. 3426–30, Aug. 2011.

Chapter 7
Conclusion and future work

In this last chapter, a summary of the contributions and conclusions of this thesis as well as future directions of this research are presented.

7.1 Conclusions

Guided by the dramatic pattern transformation of periodic elastomeric structures due to instability, the purpose of this work is to exploit this unique ability to design a flexible circuit of which the conductive pathways can be activated by a stimulus; here a load is used.

In Chapter 4, we introduced a microstructural feature, the contact nub, which enables connections when the voids compact upon buckling. We identified key geometrical features of the nubs and investigated their effects on the response of the structure through finite element analysis. It was found that parameter A (the length of intersection between the nub and the inter-void ligament) strongly affects the critical value of structure, while parameter B (the width of the mating end of the nub) and C (the distance between the opposing nubs) have little influence. Therefore, we can tune the critical stress required for buckling by changing the values of A, while tailor B for optimal conduction and C for the strain level when connection is obtained.

In Chapter 5, we analyzed the effect of adding a thin film coating based on the results of the elastomeric substrate. By running finite element simulations of structures coated with various thickness, width and stiffness, it was concluded that the stiffness of the film plays a critical role in influencing the overall buckling shape of the coated structure. For a very stiff material compared to the substrate, thickness has to be less than 1/1000 that of the substrate for the film to stretch and bend with the substrate and not to affect the buckling shape, while for a compliant film, there is a wide range of flexibility in the coating film geometry.

In Chapter 6, first we verified the validity of simulation results by comparing them with experimental results. Not only the qualitative images of different stages of deformation but also

the quantitative stress-strain curve show excellent agreement between numerical and experimental data.

Finally we applied our design principle to practice. We have successfully fabricated a flexible circuit using casting and 3D printing techniques and demonstrated the ability to activate conductive pathways via deformation-induced instabilities.

7.2 Future work

Periodic elastomeric structure is an emerging research field that is attracting growing interest for its unique properties. We have successfully demonstrated the ability to design a deformation controllable switch by exploiting the instability aspect of it. There exists tremendous opportunities for future research.

First, we designed the switch based on the simplest topology of cellular structures, a square array of circular holes on an elastomeric matrix. It has already been found that the hole shapes and hole arrangements have significant effects on the elastomer behavior. Moreover, the loading condition we have considered so far is uniaxial compression. It is interesting and desirable to explore the different responses of structures with complex topology and loading conditions, and eventually utilize them to design more sophisticated conduction pathways.

Second, we mainly focused on 2D periodic structures in this study. Analogous deformation-triggered instability should be expected in 3D periodic elastomeric structures with much more complexity and variety, which offers great potentials for the design of novel adaptive and responsive devices.

Another interesting direction of this research is to design other forms of conductive pathways. The flexible circuit we realized in this work was a result of the integration of mechanical analysis of deformation-induced surface topology change and 3D printing technology. Applications for this structure can be expanded far beyond controlling electrical conduction. Thermal, optical and acoustic conduction can also be obtained following similar approaches and offer exciting applications over a wide range of industries.

In summary, we hope this research offers some insight into the behavior of periodic elastomeric structures and serves as an important example of utilizing the unique characteristics of this structure, inspiring more exciting designs for the novel responsive and reconfigurable devices for various applications across different length scales.